

# Department of Physics and Astronomy

University of Heidelberg

Diploma thesis  
in Physics

submitted by

**Dominik Werder**

born in Hamburg

**August 2009**



**Development and Characterization  
of a Pulsed Beam  
for Neutron Decay Experiments**

**This diploma thesis has been carried out  
by Dominik Werder at the**

**INSTITUTE OF PHYSICS  
UNIVERSITY OF HEIDELBERG**

**Under the supervision of  
Professor Dr. Hartmut Abele**



**Abstract:** Precision measurements of neutron  $\beta$ -decay provide tests of the Standard Model and allow to search for physics beyond it, like left-right symmetric theories and supersymmetry. For the first time, the  $\beta$ -asymmetry correlation coefficient  $A$  was studied using a pulsed neutron beam, which has numerous advantages regarding the systematic effects. Therefore, a new low-background chopper using  ${}^6\text{LiF}$  as the absorber was developed. During the measurement, the chopped beam and the induced background effects were characterized and optimized. We show with several time of flight measurements, that the pulsed beam is advantageous for the precision of the measurement and the characterization of the instrument.

**Abstract:** Präzisionsmessungen am Zerfall freier Neutronen ermöglichen die Überprüfung des Standardmodells und die Suche nach neuer Physik, wie z.B. links-rechts-symmetrischen Theorien und Supersymmetrie. Zum ersten Mal wird für die Messung des  $\beta$ -Asymmetrieparameters  $A$  ein gepulster Neutronenstrahl verwendet. Dies bietet zahlreiche Vorteile für die Reduktion systematischer Effekte. Daher wurde für die Messung ein neuer untergrundarmer Chopper mit  ${}^6\text{LiF}$  als Absorbermaterial entwickelt. Während der Messung wurde der gepulste Strahl und der dadurch verursachte Untergrund charakterisiert und optimiert. Wir zeigen mit mehreren Flugzeitmessungen, daß der gepulste Strahl von Vorteil für die Präzision der Messung und der Charakterisierung des Instrumentes ist.



# Contents

<b>1</b>	<b>Introduction</b>	<b>3</b>
1.1	Beta-Asymmetry in Neutron Decay . . . . .	3
1.2	$V_{ud}$ and CKM Matrix . . . . .	5
1.3	Beyond the Standard Model . . . . .	5
1.4	$A$ -Measurement with PERKEO III . . . . .	6
1.5	Neutron Source . . . . .	7
1.6	Outlook . . . . .	7
<b>2</b>	<b>Beta-Decay in Pulsed Beams</b>	<b>9</b>
2.1	Motivation . . . . .	9
2.2	Neutron Absorber . . . . .	10
2.3	Chopper Variants . . . . .	11
2.4	Optimization of the Pulse Shape . . . . .	15
2.5	Material Selection . . . . .	20
2.6	Frequency Regulation . . . . .	22
2.7	Balancing and Resonances . . . . .	24
<b>3</b>	<b>Characterization of the Pulsed Beam</b>	<b>27</b>
3.1	Pulse Shape . . . . .	27
3.2	Chopper Opening Function . . . . .	28
3.3	Neutron Background at the Chopper . . . . .	32
3.4	Neutron Background on Central Solenoid . . . . .	34
3.5	Verification of the Chopper Timing . . . . .	34
3.6	Gamma-Background from the Chopper . . . . .	37
3.7	Uncertainty in Background Measurement . . . . .	37
3.8	High Energy Background . . . . .	41
3.9	Magnetic Mirror Effect . . . . .	44
3.10	B-Field Optimization . . . . .	45
3.11	Effect on the beta-Asymmetry . . . . .	47
<b>4</b>	<b>Conclusion</b>	<b>49</b>
<b>A</b>	<b>Additional Information</b>	<b>51</b>
A.1	LiF Tiles . . . . .	51
A.2	Chopper Components . . . . .	53
A.3	Frequency Regulator . . . . .	54
A.4	Vibration Measurement . . . . .	59



# Chapter 1

## Introduction

Current topics in particle physics include the observation of broken symmetries, for example of parity P, combined charge conjugation and parity CP and time reversal T. The origin of these symmetry breakings is unknown. Despite the fact, that the weak interaction in the Standard Model maximally violates parity, right handed currents could exist as a consequence of symmetry breaking during the early stages of the universe. Left-right symmetric models and Supersymmetry predict right handed currents. Moreover, the quark-mixing CKM matrix remains unexplained within the context of the Standard Model. Neutron physics provides observables which are sensitive to parity violation, right-handed currents and supersymmetric corrections, and can therefore serve as a testbed for physics beyond the Standard Model. This thesis presents a measurement with PERKEO III, a  $4\pi$  spectrometer for  $\beta$ -decay electrons. We give an overview of the available observables and the experimental setup (Chapter 1), describe the design of a new chopper system as the source of a pulsed neutron beam which is used for the measurement (Chapter 2) and analyze the pulsed beam and induced background effects (Chapter 3).

### 1.1 $\beta$ -Asymmetry in Neutron Decay

The free neutron decays by the weak interaction:

$$n \rightarrow p + e^- + \bar{\nu}_e + 782 \text{ keV} \quad (1.1)$$

Electroweak interactions are described in the standard model by a gauge theory with the gauge groups  $SU(2) \times U(1)$  and four gauge bosons, the  $\gamma$ ,  $W^+$ ,  $W^-$  and  $Z^0$ . The

Coefficient	Meaning	Current Value
$A$	$\beta$ -asymmetry	$-0.11943 \pm 0.00040$
$B$	$\bar{\nu}_e$ -asymmetry	$0.9807 \pm 0.0030$
$a$	Correlation of $e^-$ and $\bar{\nu}_e$ momentum	$-0.103 \pm 0.004$
$b$	Fierz interference, vanishes in Standard Model	-
$D$	Triple coefficient, vanishes in Standard Model	$-4 \pm 6 \cdot 10^{-4}$

Table 1.1: Some neutron decay coefficients, values from PDG 2008 [Ams08]. The value for  $A$  is taken from [Mun06].

Standard Model describes neutron decay with the parameters  $G_F$ ,  $V_{ud}$  and

$$\lambda = \frac{g_A}{g_V} = \left| \frac{g_A}{g_V} \right| e^{i\Phi} \quad (1.2)$$

where the current limit on the phase is  $\Phi = 180.06 \pm 0.07^\circ$  [Ams08]. In the case that outgoing spins are not analyzed, these parameters are related to the observables by the differential decay probability [JT57]

$$dW \propto (g_V^2 + 3g_A^2)F(E_e) \left[ 1 + a \frac{\vec{p}_e \vec{p}_\nu}{E_e E_\nu} + b \frac{m}{E_e} + \langle \vec{\sigma}_n \rangle \left( A \frac{\vec{p}_e}{E_e} + B \frac{\vec{p}_\nu}{E_\nu} + D \frac{\vec{p}_e \times \vec{p}_\nu}{E_e E_\nu} \right) \right] \quad (1.3)$$

where  $F(E_e)$  denotes the Fermi spectrum of the decay electron and  $g_V$  and  $g_A$  the vector and axial vector coupling constants of the weak interaction. The coefficients  $A$ ,  $B$ ,  $a$ ,  $b$ , and  $D$  are summarized in table 1.1. Since there are more observables than free parameters, the neutron  $\beta$ -decay provides the opportunity for precision tests of the Standard Model and physics beyond it. The ratio  $\lambda = g_A/g_V$  could in principle be calculated within the framework of QCD, but calculations using lattice QCD feature a precision of  $\pm 0.3$  on  $\lambda$  mainly due to the chiral extrapolation, which is used to get from the large low-energy cutoff to the real energy scale.  $\lambda$  can be determined from neutron decay and is required in many fields, from elementary particle physics to cosmology. The decay coefficients in equation 1.3 are related to  $\lambda$  by

$$\begin{aligned} A &= -2 \frac{\lambda(\lambda + 1)}{1 + 3\lambda^2} \\ B &= 2 \frac{\lambda(\lambda - 1)}{1 + 3\lambda^2} \\ a &= \frac{1 - \lambda^2}{1 + 3\lambda^2} \end{aligned} \quad (1.4)$$

and the measurement of the  $\beta$ -asymmetry parameter  $A$  is the most sensitive approach to determine  $\lambda$ . The relation between the angular distribution of the electrons and the decay coefficient  $A$  can be obtained from equation 1.3:

$$dW \propto 1 + \frac{v}{c} \langle \sigma_n \rangle A \cos \theta \quad (1.5)$$

An additional refinement of  $A$  comes from the weak magnetism and changes the structure of  $A$  in the following way:

$$A = A_0(1 + A_{\mu m}(A_1 W_0 + A_2 W + A_3/W)) \quad (1.6)$$

where  $A_{\mu m}$  incorporates the weak magnetism form factor,  $W$  denotes the electron energy and  $W_0$  the electron endpoint energy. The other coefficients are from [Wil82]. The expected electron-energy dependent correction on  $A$  due to the weak magnetism is on the order of  $10^{-2}$  and direct measurements by neutron decay are in sight. The form factor for the next largest correction is two orders of magnitude smaller than the weak magnetism form factor. Recent measurements of  $A$  include [Mun06, Abe02, Yer97, Lia97, Bop86].

## 1.2 $V_{ud}$ and CKM Matrix

The strong interaction eigenstates of the quarks are not eigenstates of the weak interaction. Semileptonic and hadronic current in the weak interaction therefore allow for flavor changes. Eigenstates of the strong and weak interaction are related by the Cabbibo-Kobayashi-Maskawa matrix:

$$\begin{pmatrix} |d'\rangle \\ |s'\rangle \\ |b'\rangle \end{pmatrix} = \begin{pmatrix} V_{ud} & V_{us} & V_{ub} \\ V_{cd} & V_{cs} & V_{cb} \\ V_{td} & V_{ts} & V_{tb} \end{pmatrix} \begin{pmatrix} |d\rangle \\ |s\rangle \\ |b\rangle \end{pmatrix} \quad (1.7)$$

The standard model assumes the CKM matrix to be unitary. This implies

$$|V_{ud}|^2 + |V_{us}|^2 + |V_{ub}|^2 = 1 \quad (1.8)$$

A precise measurement of the matrix elements allows for a test of the unitarity of the CKM matrix and is therefore sensitive to physics beyond the Standard Model. The contribution from  $|V_{ub}|$  is on the order of  $2 \cdot 10^{-5}$  and negligible for now.  $V_{ud}$  can be derived from neutron  $\beta$ -decay by a measurement of  $\lambda$  from one of the angular decay coefficients and the neutron lifetime  $\tau_n$ . While  $\lambda$  can be determined from an  $A$ -measurement like PERKEO III with a precision on the order of  $10^{-3}$ , the lifetime  $\tau_n$  is not yet known with the same precision. Recent measurements of  $\tau_n$  show more precise, but also inconsistent results [Mam89, Pic00, Arz00, Ser05]. A value for  $|V_{ud}|$  is obtained using  $\tau_n = 885.7 \pm 0.8$  s [Ams08] and  $\lambda = -1.2750 \pm 0.0009$  ([Abe08], average of Perkeo II measurements [Mun06, Abe97, Abe02]), and amounts to  $|V_{ud}| = 0.9751 \pm 0.0007$ . The 2008 PDG value is  $|V_{ud}| = 0.97418 \pm 0.00027$  [Ams08].

Superaligned nuclear  $\beta$ -decays  $0^+ \rightarrow 0^+$  provide another possibility to determine  $|V_{ud}|$  and to test the conserved vector current hypothesis of the Standard Model. Recent experiments result in a value of  $|V_{ud}| = 0.9738 \pm 0.0004$  [HT05].

The other input for the unitarity check ( $V_{us}$ ) is less well known and comes from Kaon and Hyperon decays. There are two values for  $V_{us}$  at the moment, depending on the form factor  $f_+(0)$  used for the evaluation. The value  $V_{us} = 0.2208 \pm 0.0027$ , derived assuming a high form factor, and  $V_{ud}$  from neutron decay doesn't violate CKM unitarity. On the other hand, using  $V_{us} = 0.2261 \pm 0.0021$  obtained with the low form factor and  $V_{ud}$  obtained from superallowed nuclear  $\beta$ -decays doesn't violate CKM unitarity either. Future measurements like PERKEO III can help to clarify this situation. A comprehensive overview can be found in [Abe08].

## 1.3 Beyond the Standard Model

The Standard Model incorporates maximal parity violation in the weak interaction. On the other hand, Grand Unified Theories assume a left-right symmetric early universe and right handed currents could be a relict of the initial left-right symmetry. A left-right symmetric expansion of the Standard Model with a gauge group  $SU(2)_L \times SU(2)_R \times U(1)$  [MP75] introduces new gauge bosons  $Z'$  and

$$\begin{aligned} W_L &= W_1 \cos \zeta + W_2 \sin \zeta \\ W_R &= e^{i\omega} (-W_1 \sin \zeta + W_2 \cos \zeta) \end{aligned} \quad (1.9)$$

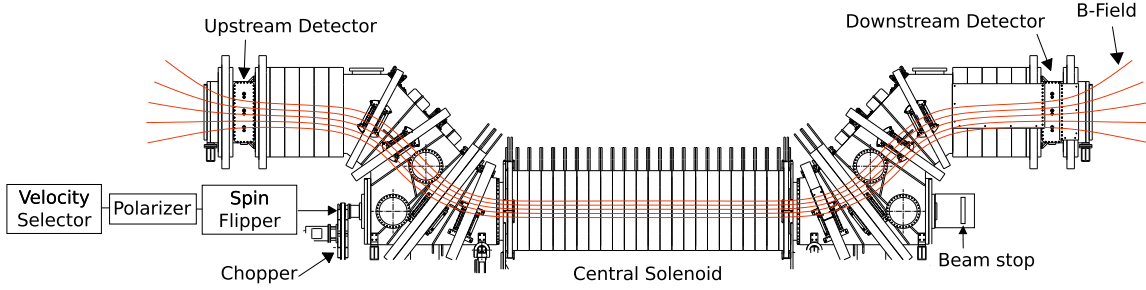


Figure 1.1: PERKEO III lateral view. Spin polarized neutrons enter the instrument from the left. The central solenoid produces a magnetic field of 150 mT which is homogeneous and has no local minima to avoid errors due to magnetic bottles and the magnet mirror effect. The magnetic field guides the decay products on spiraling tracks adiabatically to the detectors approximately 1.6 m above the beamline where only the electron energy is measured.

with the mass eigenstates  $\{W_1, W_2\}$ , the mixing angle  $\zeta$  and a CP-violating phase  $\omega$  [SBNC06]. There is a reference which constrains  $\zeta$  to  $-0.006 < \zeta < 0.0008$  [Aqu91] using neutron decay and assuming CKM unitarity.

Furthermore, the weak interaction can be searched for possible effects of supersymmetry. In order to conserve the baryon and lepton numbers, R-parity is introduced in the supersymmetric extension of the Standard Model. R-parity violating interactions affect [RMS06]

$$\lambda = \frac{g_A(0)}{g_V(0)}(1 + \Delta\hat{r}_\beta^A - \Delta\hat{r}_\beta^V) \quad (1.10)$$

Since the RPV interactions preserve the vector/axial vector structure of the low energy charged current, the contributions to  $\Delta\hat{r}_\beta^A$  and  $\Delta\hat{r}_\beta^V$  are identical and therefore not visible in  $\lambda$ . However, effects due to RPV interactions can be searched for by combining  $\beta$ -decay, Kaon semileptonic decay, B meson decay and the unitarity of the CKM matrix. Also, SUSY loop corrections can show up in  $\Delta\hat{r}_\beta^{V,A} - \Delta\hat{r}_\mu$ . Possible probes for these corrections are the neutrino asymmetry  $B$  and the Fierz term  $b$ . Effects are expected to be on the order of  $10^{-3}$ .

## 1.4 $A$ -Measurement with Perkeo III

Experiments measuring  $A$ , including PERKEO III, have the following properties in common:

- Polarized neutron beam.
- Spin flipping to measure both orientations of  $\langle\sigma_n\rangle$ .
- Measurement of  $v/c$  to be used in equation 1.5.
- Averaging over  $\cos\theta$  (Exception: [Lia97]).
- Measurement of the neutron beam's polarization.

The central distinctive property of PERKEO III is the 2.0 m long decay volume with a homogeneous magnetic field of about 150 mT. Figure 1.1 shows the setup. The beam of polarized cold neutrons coming from the left is coupled into the instrument. The magnetic field defines the quantization axis of the neutron spin and defines two hemispheres in the momentum space of the charged decay products, one in the neutron spin direction, and the other one against it. The charged decay products are guided on spiraling tracks and each hemisphere is mapped onto its own detector, which provides the averaging over  $\cos\theta$ . This allows for a  $2 \cdot 2\pi$  detection of the decay electrons with relatively small detectors, far away from background sources and with a high signal/noise ratio. Using the two  $2\pi$  detectors, PERKEO III measures

$$A_{\text{exp}}(E) = \frac{N^\uparrow(E) - N^\downarrow(E)}{N^\uparrow(E) + N^\downarrow(E)} \quad (1.11)$$

where  $N^\uparrow(E)$  denotes the electrons emitted in the hemisphere of the spin direction and  $N^\uparrow(E) + N^\downarrow(E)$  the sum of all emitted electrons, both depending on the electrons energy. One detector would be sufficient for a measurement, but a second detector allows for backscattering detection, doubles the available statistics and reduces systematic effects due to  $\gamma$ -background.

During the beam time 2008/2009, a pulsed beam is used for the first time. A neutron velocity of  $775 \pm 100$  m/s, corresponding to a wavelength of 5.1 Å, is selected with a neutron velocity selector and then shaped by a disc chopper. This allows for a virtually background free measurement during the time span when the neutron pulse is in the well defined magnetic field in the central solenoid of the instrument.

A requirement for a precise measurement with PERKEO III is the homogeneous magnetic field. A gradient in the magnetic field would decrease the measured asymmetry, since decay electrons emitted perpendicularly to the neutron spin would be mapped onto the wrong detector due to the magnetic mirror effect. Section 3.9 gives a more detailed discussion.

## 1.5 Neutron Source

The measurement with PERKEO III takes place at the Institut Laue-Langevin, Grenoble, France. The high flux reactor together with the 25 K liquid deuterium cold neutron source and the ballistic super mirror guide H113 delivers a cold neutron capture flux of  $2.0 \cdot 10^{10} \text{ cm}^{-2}\text{s}^{-1}$  [Abe06].

## 1.6 Outlook

PERC [Dub08], the successor of PERKEO III, which is currently under development, will address especially the issues regarding the magnetic field by filtering the decay products which carry only few asymmetry information. Also, the much longer decay distance increases the statistics to a large degree.



# Chapter 2

## $\beta$ -Decay in Pulsed Beams

This chapter presents the advantages of a pulsed beam for neutron decay experiments, compares the different possibilities of how to create such a beam and discusses the problems arising due to the pulsed measurement. Within the scope of this diploma thesis a new chopper system and the corresponding control electronics and software were designed, constructed and put into operation for the PERKEO III-beam time 2008/2009 at the Institut Laue-Langevin in Grenoble, France, where the setup and the chopped beam were further characterized.

### 2.1 Motivation

Previous measurements of asymmetries in the neutron  $\beta$ -decay used continuous neutron beams. Due to its length, the spectrometer PERKEO III allows for the first time measurements with a pulsed beam. The time dependency of the measurement offers numerous advantages regarding the systematic error compared to experiments using a continuous beam. First of all, the background caused by the neutron beam can be measured and is therefore deductible. Also, the signal and the background is measured under the same conditions. Moreover, the magnetic mirror effect, which causes the most important systematic correction of the instrument, can be measured as a function of the neutron pulse's time of flight. Another advantage is the improved mapping of the decay products on the detectors. During the time span when the neutron pulse is completely inside the central part of the instrument, all decay electrons are mapped on a small part of the detector which avoids fringe effects. With the additional information from the pulse clock, the events can be recorded with a time resolution of  $1\ \mu\text{s}$ . Using this additional time structure we can investigate the instrument's properties and possible background sources by far more detail than before. The spatial resolution is of course limited by the extent of the neutron pulse, as we're not able to link a decay event to a specific neutron in the pulse. Another advantage is the ability to measure changes in the ambient background caused by the other instruments because the background is measured after each pulse, that means in our case with 100 Hz. This makes the measurement more independent on external events like the opening or closing of neighboring beam shutters, thermal drifts of photomultipliers and electronics, or a change in the reactor power itself compared to experiments with a continuous beam where the beam shutter has to be manually closed for the background measurement.

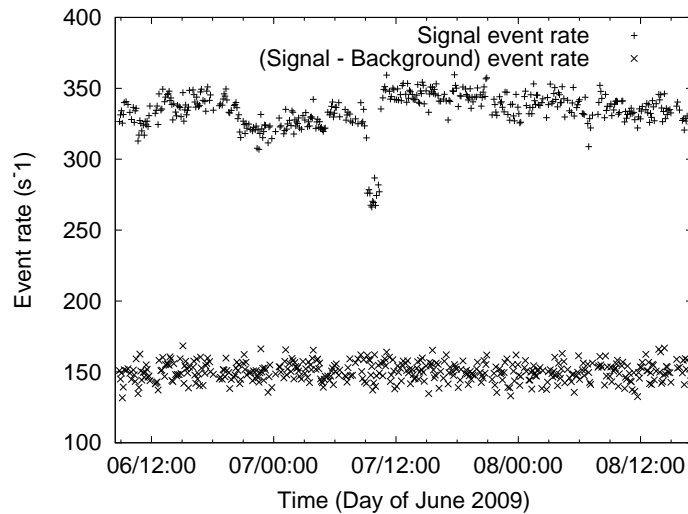


Figure 2.1: Variations in the strength of the signal. The difference of signal and background stays constant. The variations are caused by the varying background in the neutron guide hall. A pulsed beam allows for a background measurement after each pulse and takes these variations into account.

For evaluation, only the events of a specific period of time can be chosen, for example, when the neutron pulse was completely inside the homogeneous part of the magnetic field. This excludes events from the interaction of the beam with the beam stop and events produced directly or indirectly by decay electrons which are not mapped properly onto the detectors. This reduces the systematic errors considerably.

A drawback of this kind of measurement is the decrease of neutron flux by approximately 90% due to the chopper. This reduces the achievable event rate compared to a measurement using a continuous beam. Another challenge is the background generated by the chopper in close vicinity to the instrument. This background is generally time dependent and not only caused by the chopper opening itself, but also by the inhomogeneities and impurities of the neutron absorber material on the chopper disc. We therefore conducted several measurements during the begin of the beam time, in order to optimize the instrument's shielding and to show that the background generated by the chopper disc does not disturb the measurement and that signal and background are really measured under the same conditions.

## 2.2 Neutron Absorber

The neutron absorber on the chopper disc must be able to effectively absorb the neutrons while not producing too much background at the same time, since the position of the chopper in close vicinity to the upstream detector doesn't leave much space for additional shielding. Moreover, the material has to withstand the high mechanical strain and should be easy to process. We'll give an overview on the different options and discuss their advantages and drawbacks.

**Gadolinium:**  $^{157}\text{Gd}$  features with  $2.59 \cdot 10^5$  barn the largest cross section for cold neutrons of all known nuclei, while  $^{155}\text{Gd}$  has  $6.11 \cdot 10^4$  barn. Natural Gadolinium has a cross section of  $4.97 \cdot 10^4$  barn and is a very effective neutron absorber. One severe issue with Gadolinium is that every neutron capture produces high energy  $\gamma$  and on average one electron by internal conversion [HM52]. The electron energy spectrum consists of several peaks at 71, 81, 130, 147 and 172 keV [RGF67]. The  $\gamma$  background is produced by several reactions resulting in cascades with a total energy of 7.9 MeV for  $^{157}\text{Gd}$  and 8.5 MeV for  $^{155}\text{Gd}$ , which is why Gadolinium is also used in detectors for cold neutrons. For PERKEO III, the generated background is too high.

**Boron carbide:** The cross section of  $^{10}\text{B}$  for cold neutrons is 3835 barn [ILL03]. Every neutron capture produces  $\gamma$  though, which are difficult to shield due to the chopper's position underneath the detector vessel. Another drawback of  $^{10}\text{B}_4\text{C}$  is its hardness, which has a 9.3 on the Mohs scale and is among the hardest known materials, only surpassed by boron nitride and diamond, which renders it very difficult to process. If shielding is not an issue,  $^{10}\text{B}_4\text{C}$  has the advantage that it is more easily available than other isotopes.

**Aluminium diboride:**  $\text{AlB}_2$  is more soft than boron carbide, but the aluminium produces unwanted  $\gamma$ -background though. Aluminium dodecaboride ( $\text{AlB}_{12}$ ), would have a higher fraction of boron, but the material is like  $\text{B}_4\text{C}$  very hard and therefore difficult to process.

**Lithium fluoride:** The cross section for cold neutrons of  $^6\text{Li}$  is 940 barn. Neutrons interact with  $^6\text{Li}$  by



with the tritium receiving a maximum energy of 2.73 MeV. The tritium triggers together with Li, F, C, H and O a chain of secondary reactions, which can produce  $\gamma$  and fast neutrons [Lon80]. The fast neutrons are more problematic than the  $\gamma$ -background, in that they are moderated in the cooling water of the magnets and can cause a time dependent background structure. The  $\gamma$  production, on the other hand, is suppressed by  $10^{-4}$  compared to  $^{10}\text{B}_4\text{C}$ . Using the molar volume  $V_m = 12.11 \text{ cm}^3/\text{g}$  of LiF, we get an attenuation length of

$$x_0 = 0.428 \text{ mm} \quad (2.2)$$

which, using 4 mm  $^6\text{LiF}$  as the absorber, corresponds to a transmission coefficient of  $8.8 \cdot 10^{-5}$ . Lithium fluoride can be processed with existing tools.

Due to the chopper's position near the upstream detector, we use  $^6\text{LiF}$  as the neutron absorber in order to keep the additional  $\gamma$  background, produced by the chopper, as low as possible. With an additional gadolinium coating on the back side, the transmission coefficient for cold neutrons decreases even more. The manufacturing of pure  $^6\text{LiF}$  tiles, which are stable enough for the use in a chopper disc turning at 100 Hz, is not straightforward, and was optimized within the scope of this work. Detailed results are presented in section A.1.

## 2.3 Chopper Variants

There are several basic chopper designs, which we will briefly discuss:

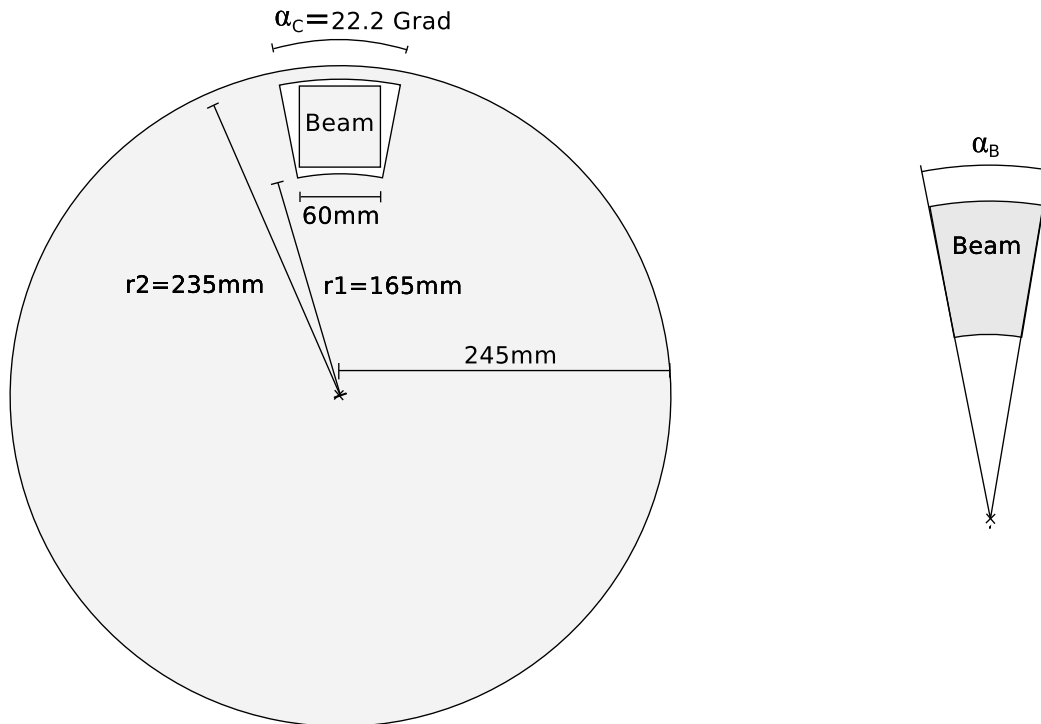


Figure 2.2: Disc chopper with chopper window and beam profile. The left diagram shows the chopper geometry, which was realized for the PERKEO III beam time. Noticeable here is, that the beam profile fits completely within the inner and outer radius of the chopper window, which allows for a simpler neutron absorber design, since the outer and inner radii of the chopper window don't have to be covered. For the timing calculations, we assume that the beam itself is shaped like a sector of a circle, as shown in the right part of this figure. The implications of the real geometry are taken into account for the theoretical calculation of the pulse in section 3.2.

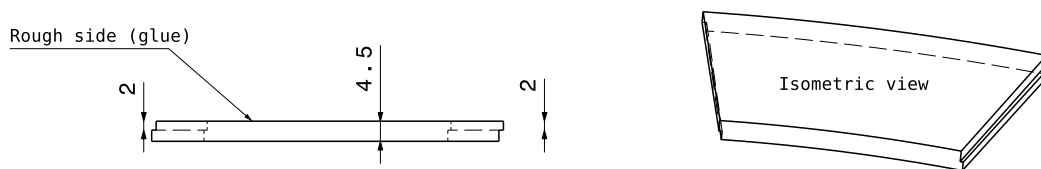


Figure 2.3: The  ${}^6\text{LiF}$  tiles are produced with a step so that neighboring tiles overlap each other in order to avoid gaps in the absorber, but the steps don't touch to avoid any load on the fragile edges of the tiles. Care must be taken, since the speed of the tiles at the mean radius of 200 mm is  $118 \text{ m/s}$ , which is 15% of the neutron velocity. A beveling of the tiles with the wrong inclination would open a gap for the neutrons.



Figure 2.4: The finished chopper disc. One can see the  ${}^6\text{LiF}$  tiles used as the neutron absorber, the chopper opening angle of  $\alpha_C = 22.11^\circ$  and the balancing weights made of copper. The joints between the tiles feature a slight step which guarantees a maximum neutron transmission of  $8.8 \cdot 10^{-5}$ .

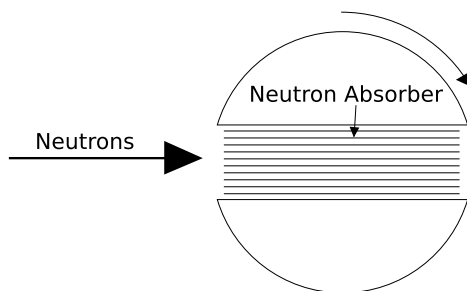


Figure 2.5: Fermi chopper, consisting of a rotating cylinder with sheets of neutron absorbing material. More sheets create sharper pulses at the same rotary frequency, but sheets have to be thin in order to not decrease flux density too much.

**Disc chopper:** A disc chopper consists of a rotating disc coated with a neutron absorber. One or more windows in the disc allow the beam to pass through for a short period of time. The pulse shape is defined by the disc's rotation frequency and the chopper opening window, as shown in figure 2.2. It is possible to create an even better defined pulse with steeper slopes by combining two disc choppers which rotate in opposite directions, without having to build a disc with a larger diameter or by using higher frequencies.

**Fermi chopper:** A Fermi chopper consists of an array of neutron absorbing plates, stacked with some spacing on top of each other, which rotate on an axis perpendicular to the beam axis. The Fermi chopper has the advantage, that it can produce short pulses with a relatively low rotary frequency using many sheets of absorption material (figure 2.5). However, since the absorbing sheets stay within the beam, they have to be as thin as possible, which can't be achieved with polycrystalline  ${}^6\text{LiF}$ , but for example with cadmium or gadolinium coated aluminium.

**${}^3\text{He}$ -Cell:** Polarized  ${}^3\text{He}$  absorbs neutrons with the matching polarization. It is therefore possible to create a chopped beam using polarized neutrons and a spin flipper. A big advantage is that one doesn't have to construct heavy rotating parts and that the pulse shape can be varied quickly. One drawback is, that the imperfect polarization of the beam allows neutrons to pass the chopper even when it is in closed mode. Another drawback is the fringe effect due to neutrons passing the  ${}^3\text{He}$  chopper during a spin flip change. These effects reduce the overall polarization of the pulses. Also, the  ${}^3\text{He}$  has to be re-polarized on a regular basis. As long as no possibilities exist to re-polarize the  ${}^3\text{He}$  in place, this would cause a time dependent chopper efficiency. In contrast, with an in situ polarization mechanism, one would be able to design a very flexible chopper system.

Out of these options, we've chosen the disc chopper variant which is well suited for the large beam cross section of  $60\text{ mm} \times 60\text{ mm}$  and allows a compact design in order to minimize the distances between the beam apertures.

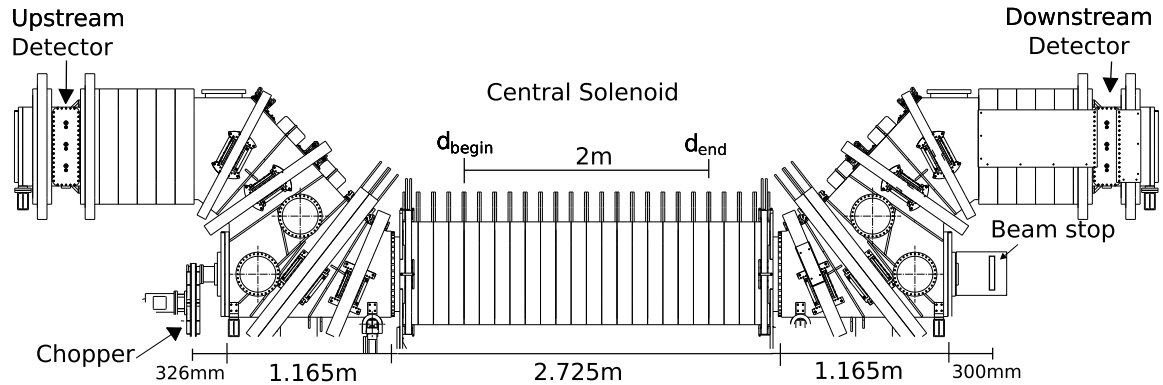


Figure 2.6: Distances used for the calculation of the chopper timing. The signal measurement takes place when the neutron pulse is completely inside the central decay volume, denoted by  $d_{\text{begin}}$  and  $d_{\text{end}}$ . Background is measured after the neutron pulse is fully absorbed by the beam stop.

## 2.4 Optimization of the Pulse Shape

The purpose of the chopper is to create neutron pulses with a defined length and keep the instrument free of neutrons for a specified time in order to measure the background. Figure 2.7 shows the propagation of a neutron pulse during one chopper cycle. The time span which is available for the measurement starts, when the slowest neutrons from the end of the pulse reach the part of the instrument where the homogeneous magnetic field begins, and stops, when the fastest neutrons from the beginning of the pulse reach the end of the homogeneous magnetic field. The extent of the neutron pulse must therefore be smaller than the length of the homogeneous part of the instrument. A long pulse contains more neutrons and provides a higher decay rate. On the other hand, a short pulse would yield the longest possible time to measure the decays. Therefore, there is an optimum for the chopper geometry which is determined in section 2.4. There is also an optimal ratio between the time which is available for the signal and the background measurement [Kno79]. This is given by the event rates of signal and background:

$$\frac{t_s}{t_b} = \sqrt{\frac{c_s}{c_b}} \quad (2.3)$$

where  $t_s$  and  $t_b$  are the signal and background measurement time spans and  $c_s$  and  $c_b$  the signal and background event rates, respectively, where signal is the sum of the foreground and background:

$$c_s = c_f + c_b \quad (2.4)$$

We estimated from the results of the first measurement with PERKEO III, that  $c_s \approx 2c_b$ , therefore

$$\frac{t_s}{t_b} = \sqrt{2} \quad (2.5)$$

This was also confirmed during the current measurement with  $S/N \approx 2.1$ .

The chopper opening function  $A_{\text{open}}(t)$  is the convolution of the chopper window and the aperture in front of the chopper. For this calculation we can describe both

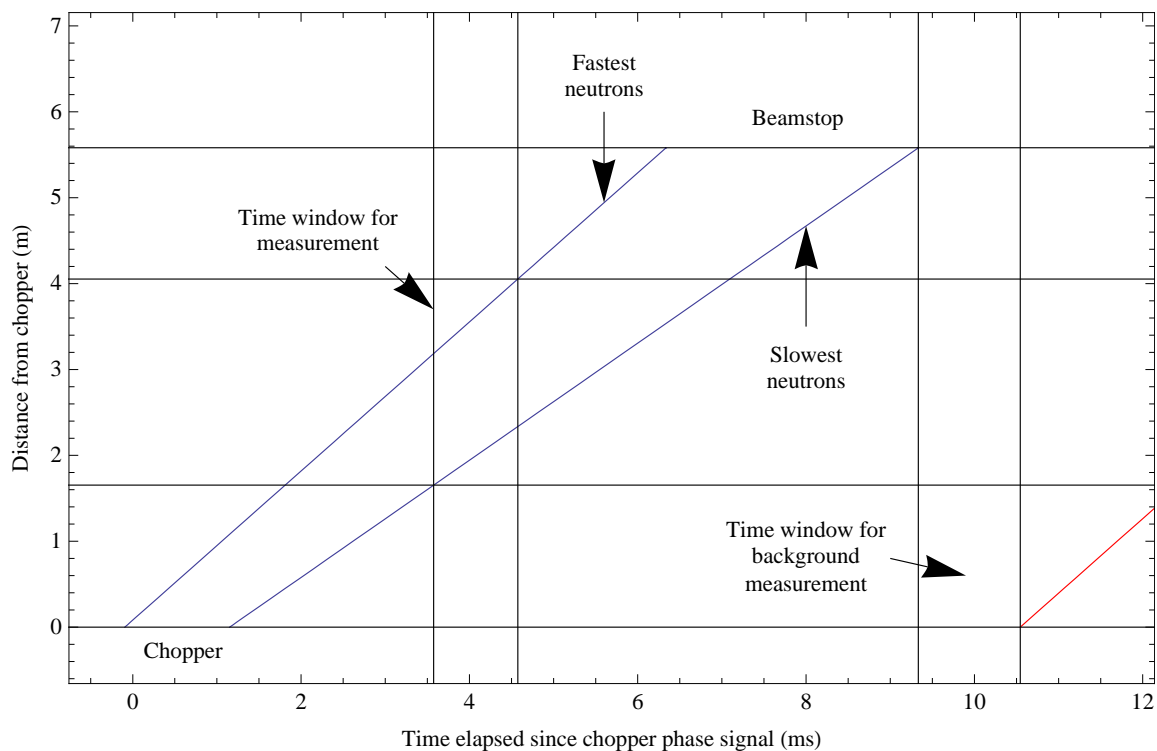


Figure 2.7: Timing diagram of one neutron packet moving through the instrument. The zero on the time axis indicates the chopper trigger signal. Drawn are the path of the fastest neutrons from the beginning of the pulse and the path of the slowest neutrons from the end of the pulse. The measurement of the signal takes place during the time when the pulse fits completely inside the center part of the instrument. After the pulse is fully absorbed by the beam stop, the background is measured until the next chopper opening. The red line shows the beginning of the next pulse.

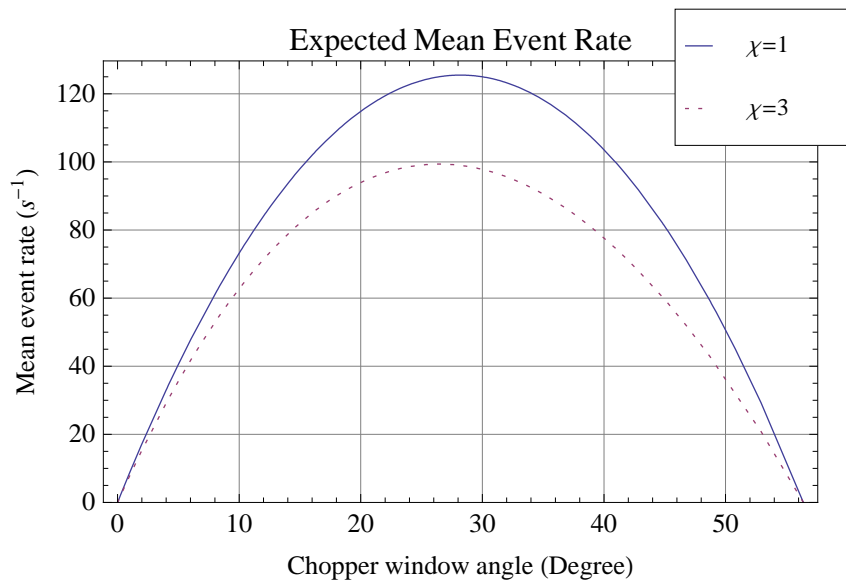


Figure 2.8: Expected mean neutron decay rate in PERKEO III as a function of the chopper opening window.  $\chi$  denotes the ratio of the time spans for the background and signal measurement. The solid line assumes a background measurement of equal length as the signal measurement ( $\chi = 1$ ). The dotted line assumes a background measurement three times as long ( $\chi = 3$ ). This plot uses the actually realized experimental setup, see table 2.1. The optimum chopper window angle depends on  $\chi$ , but this dependency is not too strong and the same chopper disc can be used with different ratios of signal and background measurement time.

the chopper window and the aperture by rectangular functions, which means that both openings are shaped like a sector of a circle. The exact opening function will be calculated in section 3.2 and will be used to compare the data obtained from the time of flight measurement with the theoretical pulse. During one pulse, the chopper window is open for some integrated angular seconds  $\Omega$ , given by the angle of the chopper window  $\alpha_C$  (Figure 2.2), the angle of the aperture  $\alpha_B$  and the rotary frequency  $f$ :

$$\Omega = \frac{\alpha_C \alpha_B}{2\pi f} \quad (2.6)$$

With the inner and outer radii of the chopper window  $r_1$  and  $r_2$ , and the neutron flux density  $j_0$ , this yields the number of neutrons contained in one pulse:

$$\begin{aligned} N &= \frac{\Omega}{2} (r_2^2 - r_1^2) j_0 \\ &= \frac{\alpha_C \alpha_B}{4\pi f} (r_2^2 - r_1^2) j_0 \end{aligned} \quad (2.7)$$

The time span  $t_m$  which is available for the signal measurement during one pulse, is the time that the pulse spends inside the homogeneous part of the magnetic field, compare figure 2.7. It is given by

$$t_m = \frac{d_{\text{end}}}{v_{\text{max}}} - \frac{d_{\text{begin}}}{v_{\text{min}}} - t_{\text{open}} \quad (2.8)$$

where we use the distances  $d_{\text{begin}}$  and  $d_{\text{end}}$  from the chopper disc to the beginning and the end of the measurement volume, respectively (figure 2.6), the maximum and minimum velocities of the neutrons  $v_{\text{max}}$  and  $v_{\text{min}}$ , and the time  $t_{\text{open}}$  during which neutrons can pass the chopper. The chopper opening time  $t_{\text{open}}$  depends on the angle of the chopper window, the angle of the beam aperture, and the rotary frequency  $f$ , as in

$$t_{\text{open}} = \frac{\alpha_C + \alpha_B}{2\pi f} \quad (2.9)$$

The length of one chopper pulse period is therefore determined by the time  $t_{\text{open}}$ , the time that the neutrons need to reach the beam stop, and the time span  $\chi t_m$ , during which we want to measure the background, where  $\chi$  is a dimensionless constant. The distance  $d_{\text{stop}}$  is the distance from the chopper to the beam stop. The rotary frequency is therefore given by:

$$\begin{aligned} \frac{1}{f} &= t_{\text{open}} + \frac{d_{\text{stop}}}{v_{\text{min}}} + \chi t_m \\ &= \frac{\alpha_C + \alpha_B}{2\pi f} + \frac{d_{\text{stop}}}{v_{\text{min}}} + \chi \left( \frac{d_{\text{end}}}{v_{\text{max}}} - \frac{d_{\text{begin}}}{v_{\text{min}}} - \frac{\alpha_C + \alpha_B}{2\pi f} \right) \end{aligned} \quad (2.10)$$

We define the effective length of the decay volume

$$\gamma = \frac{v_{\text{min}}}{v_{\text{max}}} d_{\text{end}} - d_{\text{begin}} \quad (2.11)$$

and find the equation for the chopper frequency:

$$f = v_{\text{min}} \frac{1 - \frac{\alpha_C + \alpha_B}{2\pi} (1 - \chi)}{d_{\text{stop}} + \chi \gamma} \quad (2.12)$$

The actual mean event rate  $g$  available for the measurement is, using the lifetime of the neutron  $\tau = 885.7$  s [Ams08] and the neutron flux density  $j_0$ :

$$\begin{aligned} g &= \frac{N}{\tau} t_m f \\ &= \frac{\alpha_C \alpha_B}{4\pi f} (r_2^2 - r_1^2) \frac{j_0}{\tau} \left( \frac{d_{\text{end}}}{v_{\text{max}}} - \frac{d_{\text{begin}}}{v_{\text{min}}} - \frac{\alpha_C + \alpha_B}{2\pi f} \right) \end{aligned} \quad (2.13)$$

and can be written in terms of the chopper window's angle  $\alpha_C$  using equation 2.12:

$$g = \frac{\alpha_C \alpha_B}{4\pi} (r_2^2 - r_1^2) \frac{j_0}{\tau v_{\text{min}}} \left( \gamma - \frac{d_{\text{stop}} + \chi\gamma}{\frac{2\pi}{\alpha_C + \alpha_B} - 1 + \chi} \right) \quad (2.14)$$

This dependency is shown in figure 2.8 for a measured neutron capture flux density of  $j_0 = 1.1 \cdot 10^8 \text{ s}^{-1} \text{ cm}^{-2}$  which was measured by a gold foil activation. Using equation 2.14 we can find the optimal chopper opening window by maximizing the event rate with respect to  $\alpha_C$ . We ignore the constants and find

$$\frac{dg}{d\alpha_C} = \gamma - \frac{d_{\text{stop}} + \chi\gamma}{\frac{2\pi}{\alpha_C + \alpha_B} - 1 + \chi} - \frac{2\pi\alpha_C}{(\alpha_C + \alpha_B)^2} \frac{d_{\text{stop}} + \chi\gamma}{\left(\frac{2\pi}{\alpha_C + \alpha_B} - 1 + \chi\right)^2} \quad (2.15)$$

For an equal signal and background measurement time span,  $\chi = 1$ , this reduces to

$$\begin{aligned} 0 &= \gamma - \frac{d_{\text{stop}} + \gamma}{\frac{2\pi}{\alpha_C + \alpha_B}} - \frac{2\pi\alpha_C}{(\alpha_C + \alpha_B)^2} \frac{d_{\text{stop}} + \gamma}{\left(\frac{2\pi}{\alpha_C + \alpha_B}\right)^2} \\ \alpha_C &= \frac{\pi\gamma}{d_{\text{stop}} + \gamma} - \frac{\alpha_B}{2} \end{aligned} \quad (2.16)$$

while for  $\chi \neq 1$  we find the solution

$$\alpha_C = 2\pi \frac{-1 + \sqrt{1 + \frac{\chi-1}{d_{\text{stop}} + \gamma} (\gamma + \frac{\alpha_B}{2\pi} (d_{\text{stop}} + \chi\gamma))}}{\chi - 1} - \alpha_B \quad (2.17)$$

We see from equation 2.14 that a very effective way to increase the event rate would be to increase the length of the decay volume. In fact, defining

$$c_0 = \frac{2\pi}{\alpha_C + \alpha_B} - 1 + \chi \quad (2.18)$$

we see, that in order to increase the event rate by a factor of  $\Phi$ , we have to change  $\gamma$  by a factor of  $\xi$  given by

$$\frac{g_2}{g_1} = \Phi = \frac{\xi\gamma - \frac{\chi\xi\gamma}{c_0} - \frac{d_{\text{stop}}}{c_0}}{\gamma - \frac{\chi\gamma}{c_0} - \frac{d_{\text{stop}}}{c_0}} \quad (2.19)$$

resulting in

$$\xi = \Phi - \frac{d_{\text{stop}}(\Phi - 1)}{\gamma(c_0 - \chi)} \quad (2.20)$$

Now we calculate how much longer the decay volume must be to increase the event rate. Here, we make the assumption that we extend the central homogeneous part of

the instrument symmetrically to both sides without changing the total length of the instrument. The equation

$$\xi\gamma = \frac{v_{\min}}{v_{\max}} \left( d_{\text{end}} + \frac{\sigma}{2} \right) - \left( d_{\text{begin}} - \frac{\sigma}{2} \right) \quad (2.21)$$

where  $\sigma$  is the total extension of the central decay volume, leads to

$$\sigma = 2(\Phi - 1) \frac{\gamma - \frac{d_{\text{stop}}}{\frac{2\pi}{\alpha_C + \alpha_B} - 1}}{\frac{v_{\min}}{v_{\max}} + 1} \quad (2.22)$$

Using the values from the current setup

$$\begin{aligned} \alpha_C &= 22.1^\circ \\ \alpha_B &= 20.0^\circ \\ d_{\text{stop}} &= 5.68 \text{ m} \\ \gamma &= 1.53 \text{ m} \\ v_{\max} &= 876 \text{ m/s} \\ v_{\min} &= 674 \text{ m/s} \end{aligned} \quad (2.23)$$

we find an equation for the extension of central homogeneous part in terms of  $\Phi$

$$\sigma = 0.87 \text{ m} \cdot (\Phi - 1) \quad (2.24)$$

therefore, to double the event rate, one would have to extend the central decay volume by a total of 87 cm.

The optimal chopper disc geometry has been calculated based on the assumptions of the beam line setup and the anticipated length of the homogeneous decay volume (Section 3.9). The layout of the beam line changed a bit on site and the length of the homogeneous magnetic field is 0.4 m longer than anticipated. Table 2.1 lists the theoretical values for the optimal chopper frequency and chopper window angle depending on the parameters that changed between planning and experimental setup. The longer distance of the decay volume has the biggest influence on the higher realized event rate, even though the chopper opening angle is not the optimum for the realized setup. Despite that, a shorter pulse has the advantage that it decreases the correction caused by the magnetic mirror effect.

## 2.5 Material Selection

The chopper's frequency of 100 Hz places high demands on the material for chopper disc. Acceleration as high as 9860 times the earth's own gravitation acts on the edge of the disc when spinning at full speed. At the same time must the material be suitable for a vacuum up to  $10^{-6}$  mbar.

We've chosen a diameter of 490 mm for the chopper disc, since it fits underneath the experiment and we also can use an existing vacuum vessel. The required tensile strength of the disc material results from the centrifugal force acting on the disc. We

	Planned	Actual Setup
Distance of chopper to PERKEO III (m)	0.230	0.326
Length of homogeneous volume (m)	2.000	2.400
Distance from end of PERKEO III to beam stop (m)	0.230	0.300
Optimal chopper window angle for $\chi = \sqrt{2}$ ( $^\circ$ )	22.11	28.21
Optimal chopper frequency (Hz)	92.9	94.6
Max. event rate with optimal $\alpha_C$ and $f$ (Hz)	78	125
Realized chopper window ( $^\circ$ )	22.11	22.11
Measured rate with $\alpha_C = 22.11^\circ$ and $f = 94$ Hz (Hz)	-	115

Table 2.1: Comparison between the planned and realized beamline setup and the resulting chopper performance.

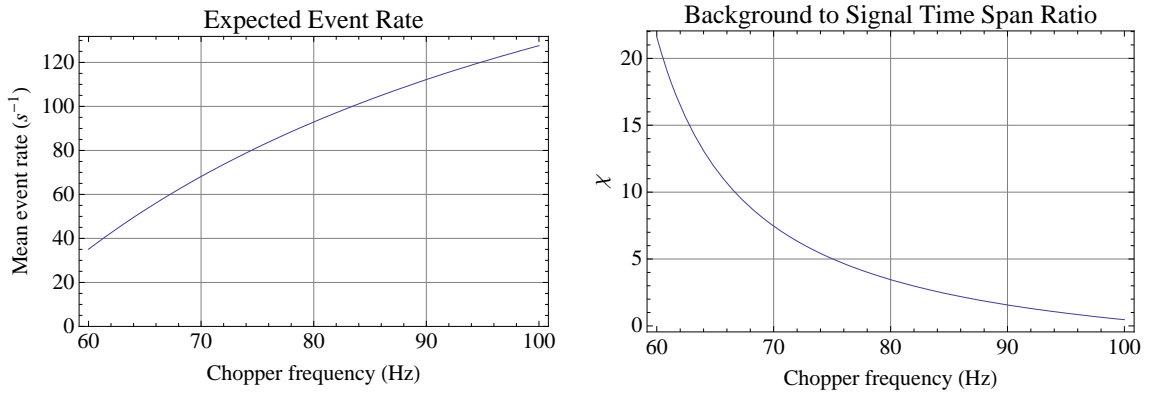


Figure 2.9: The expected event rate and the background to signal measurement time ratio  $\chi$  for the realized chopper disc with  $\alpha_C = 22.1^\circ$  assuming the actually realized experimental setup (table 2.1).

consider a infinitesimal volume of the disc, from the inner radius  $r_1$  to the outer radius  $r_2$ , with a thickness  $D$ :

$$V = \frac{\pi(r_2^2 - r_1^2)}{2\pi} D d\phi \quad (2.25)$$

The surface of this volume element at the inner radius is

$$A = \frac{2\pi r_1}{2\pi} D d\phi \quad (2.26)$$

Then we use the density  $\rho$  and the chopper frequency  $f$  to calculate the force acting on the surface element at the inner radius:

$$\frac{F}{A} = 2\pi^2 \rho(r_2^2 - r_1^2) f^2 \quad (2.27)$$

Table 2.5 lists the tensile strengths of some materials and gives the maximum possible diameter of a chopper disc, excluding any safety margin:

Material	Tensile strength N/mm <sup>2</sup>	max. diameter m
Steel	500	1.1
Aluminium	350	1.6
Fiber reinforced plastic	600	2.2
Carbon reinforced plastic	1500	4.0

Of these materials, the fiber reinforced plastic turns out to be best suited for this application. The other materials feature a high electrical conductivity which would disturb the magnetic field and could influence the neutron polarization. Using composite materials, it is also important to note that the high tensile strength is only provided in the direction of the fibers.

## 2.6 Frequency Regulation

The precision of the frequency influences directly the quality of the time of flight measurements, since the lengths of the neutron pulses change with the frequency. Averaging the time of flight data over different frequencies blurs the spectrum. We therefore want a frequency regulation which has a maximum relative deviation of  $10^{-3}$ , is stable to most other external events, like temperature drifts and changes in power supply voltages, and provides some facility to easily operate and automatically monitor the chopper. We tested the existing proportional regulation for the chopper motor, which uses a frequency to voltage converter to control the power supply's output voltage. A measurement of the stability was conducted over a period of 10 hours. The output of the frequency to voltage converter was recorded and compared with the rotary frequency measured with an external pulse counter. The signal of the F/V converter, scaled to Hz, is shown in figure 2.10.

It is visible that the missing integral part of the regulation causes major drifts in the frequency. The frequency mean value changes during the night by up to 1.0%, which would blur the time of flight measurement due to varying neutron packet lengths. Also, there is a high amount of noise on the signal, probably caused by the frequency to voltage converter.

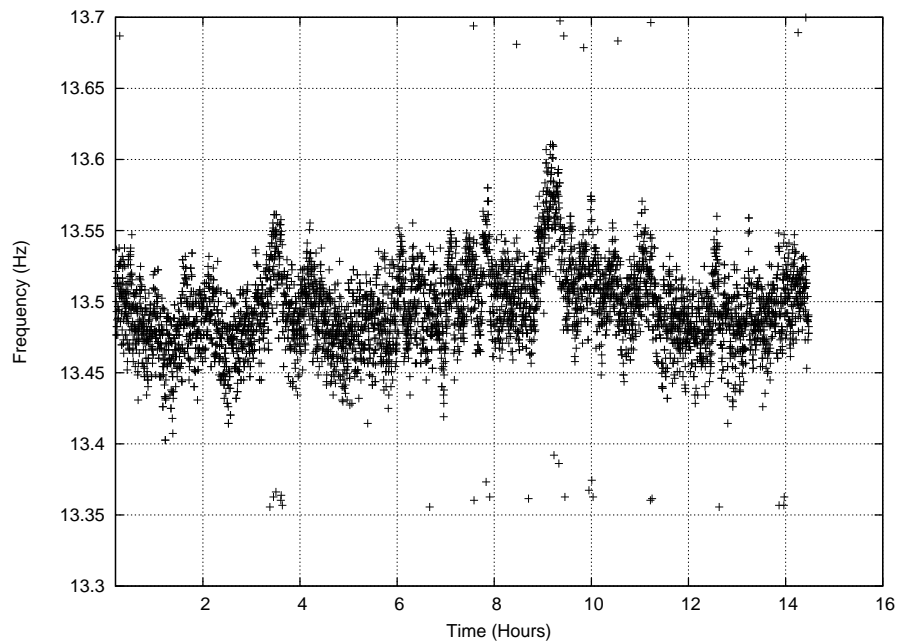


Figure 2.10: Chopper frequency measured during one night using the old regulator. We see a uncertainty in the measurement of 0.4% and drifts of more than 1%. The long term stability can not be guaranteed.

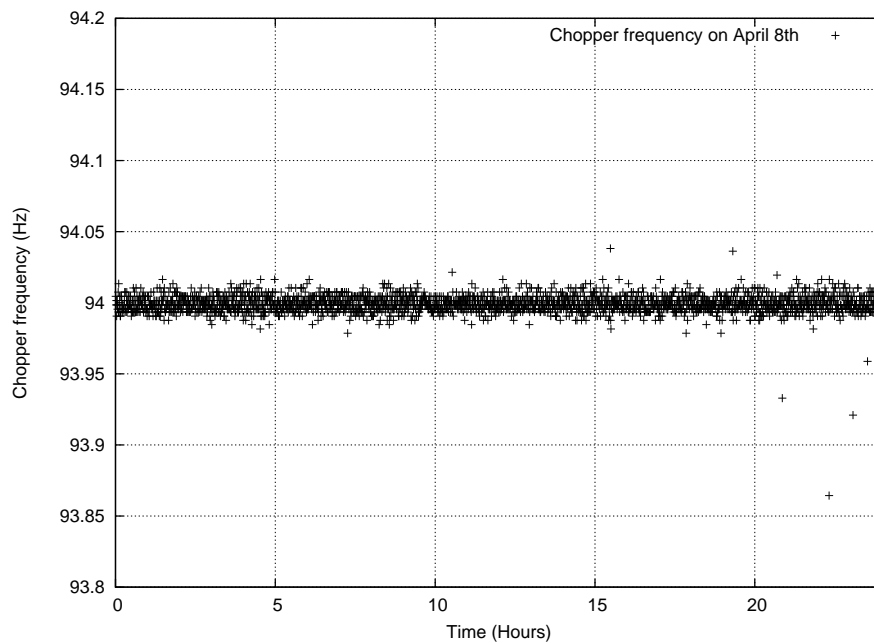


Figure 2.11: Time evolution of the chopper's frequency using the new regulation, as measured on April 8th 2009. The frequency stays constant with a FWHM of 0.012 Hz. Long-term stability can be guaranteed which improves the resolution of the time of flight measurements.

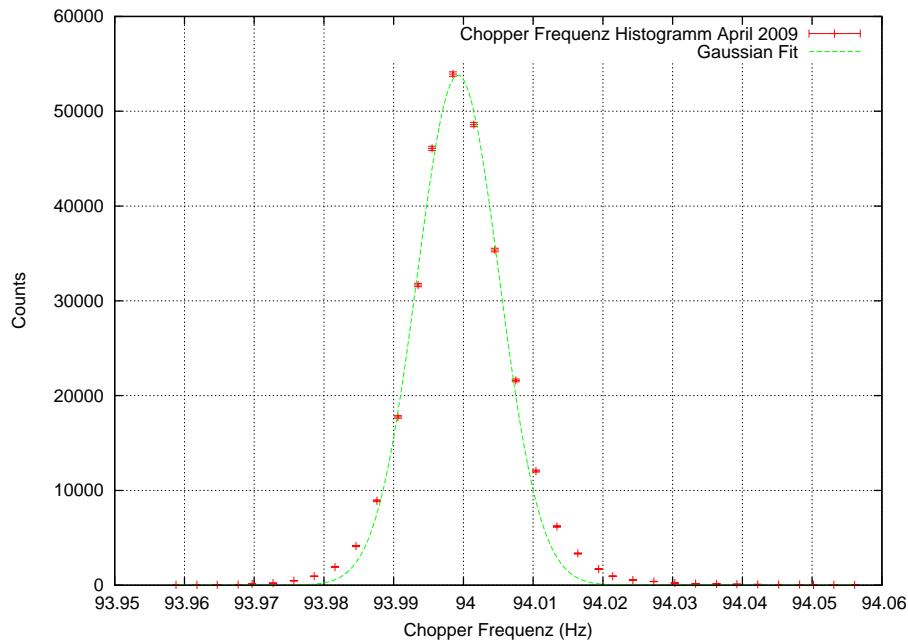


Figure 2.12: Histogram of the chopper frequencies measured during April. The frequency is measured every 3 seconds. We achieve a FWHM of 0.012 Hz. The Gaussian fit serves to guide the eye of the reader and does not describe the data well for larger frequency deviations because the deviations are not randomly distributed.

We decide to use a new chopper regulator based on a microcontroller in order to achieve a higher accuracy. The microcontroller counts the chopper's frequency and uses a quartz crystal for timing which makes it independent of the high temperature drifts at the beam site. With the new regulation we achieve a much higher precision and see no long-term drifts in frequency at all. The time evolution of the frequency of one night is drawn in figure 2.11 and a histogram of all measured frequencies during April 2009 is shown in figure 2.12. We achieve a FWHM of 0.012 Hz ( $2.1 \cdot 10^{-4}$  relative). More details on the new regulation are given in section A.3.

## 2.7 Balancing and Resonances

The chopper was balanced up to a quality factor of  $G = 6.3 \text{ mm/s}$ , which indicates a maximum speed of the disc's center of mass. The relation between  $G$  and the force acting on the bearing is

$$F = 2\pi f m G \cdot 10^{-3} \quad (2.28)$$

where  $f$  is the rotary frequency and  $m = 4.1 \text{ kg}$  the disc mass. This gives a maximum force on the bearing of 16.2 N at  $f = 100 \text{ Hz}$  assuming that the bearing has no tolerance at all. At the same time,  $G = 6.3$  means that the disc's center of mass moves at  $f = 100 \text{ Hz}$  on a radius  $r$  given by

$$r = \frac{G}{2\pi f} = 10 \mu\text{m} \quad (2.29)$$

---

The tolerance of the bearing is clearly larger and can compensate for the residual imbalance, provided that there are no resonances. With the kind support of the ILL, we performed a chopper test run up to the designated maximum nominal frequency of 100 Hz while monitoring the vibration at two points of the chopper case. At this frequency, the disc has a kinetic energy of 24.3 kJ. This test was successfully completed and the system received clearance from the ILL security staff. The appendix contains the results of the measurements. The vibration is automatically monitored during chopper operation and the chopper is shut down if any of these values raises above a threshold. During the whole beam time, all parameters stayed inside their safety margins and the chopper was never shut down due to a fault condition.



# Chapter 3

## Characterization of the Pulsed Beam

The pulsed beam gives rise to new background effects which can affect the measurement. Within the scope of this work, these effects were analyzed with several time of flight measurements. These measurements and evaluations were conducted while the experiment was still in progress and are used to further optimize the current setup.

### 3.1 Pulse Shape

In order to characterize the new chopper system and to validate the theoretical calculations, we conduct a time of flight measurement to measure the time dependent propagation of the neutron pulses through the instrument. For this measurement we put two 0.2 mm thick aluminium foils inside the central vessel of PERKEO III symmetrically to the center of the instrument and perpendicularly with a distance of 2 m to each other. The corresponding detectors are two sodium iodide scintillation counters mounted outside of the vacuum underneath the aluminium foils and covering a solid angle of 0.020. Aluminium has a cross section for cold neutrons of  $2.335 \cdot 10^{-1}$  barn and can be activated by neutrons under spontaneous emission of  $\gamma$  according to



and decays into



With the NaI counters, we measure mostly the spontaneous  $\gamma$  emitted by the activated Al foils. An example of such a measurement is shown in figure 3.1. Assuming that the neutron flux density is constant over the velocity range used in our experiment, we can use the time difference between the  $\gamma$  peaks to calculate the mean velocity of the neutrons. The results of this measurement are shown in figure 3.2. The error on this measurement is dominated by the errors on the aluminium foils' positions, which have an accuracy inside the instrument up to  $\pm 7$  mm. The mean velocity is  $707.1 \pm 0.4$  m/s, corresponding to a de Broglie wavelength of  $5.59 \text{ \AA}$ .

The readout electronics of PERKEO III uses the trigger signal of the chopper to reset the timer counters. It is therefore important for the data evaluation to know the angle between the trigger signal and the position of maximum transmission of the

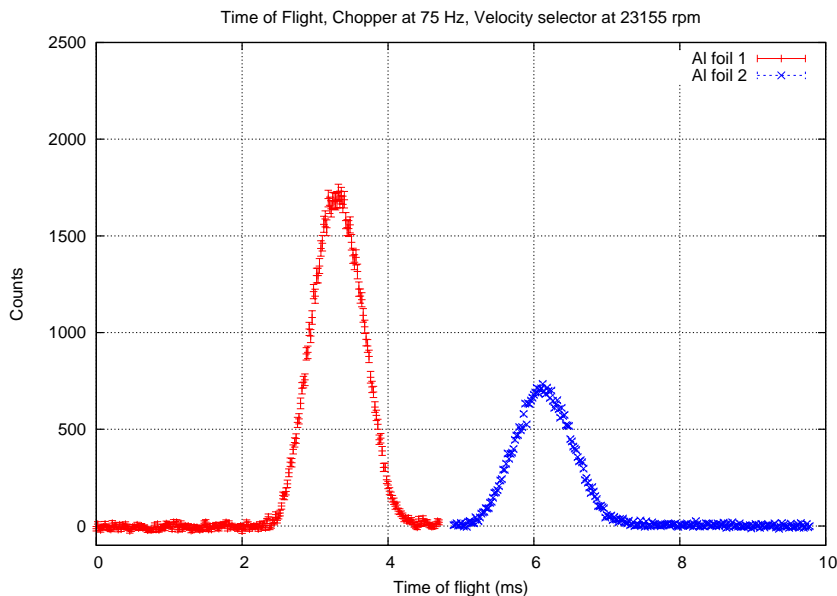


Figure 3.1: Time of flight measurement using two thin aluminium foils inside of PERKEO III and two  $\gamma$  scintillation counters directly underneath the foils, but outside of the vacuum. The data on the left half is from Al foil 1 (upstream), the right half from Al foil 2 (downstream). The time axis is the elapsed time since the chopper trigger signal. The detectors were not calibrated, so the amplitudes may not be compared.

disc. We can find this angle  $\alpha_{\text{off}}$  from the time of flight measurement by observing that the time of flight of the neutron pulse's maximum to one of the Al foils is given by

$$t = \frac{\alpha_{\text{off}}}{2\pi f} + \frac{d}{v} \quad (3.3)$$

with the unknown angle  $\alpha_{\text{off}}$ , the chopper frequency  $f$ , the distance from the chopper to the aluminium foil  $d$  and the mean velocity of the neutrons  $v$ , determined in figure 3.2. The fit of this measurement and the results for both detectors are shown in figure 3.3. In this calculation, we assume that the trigger signal generated by the chopper does not depend on the rotary frequency itself but only on the angle between the chopper trigger signal and the disc's position of maximum transmission.

In order to calibrate the neutron velocity selector, we repeat the time of flight measurements for different selector settings. The same selector speed was always measured twice, during ramp-up and ramp-down. The errors are dominated by the uncertainties in the positions of the Al foils. We expect a linear relation between the rotary frequency of the velocity selector and the neutron's mean velocity. The results are shown in figure 3.4 and confirm the theoretical expectations very well.

## 3.2 Chopper Opening Function

In this section we calculate the predicted neutron pulses using a more detailed chopper opening function and fit them to the time of flight data to test the theoretical

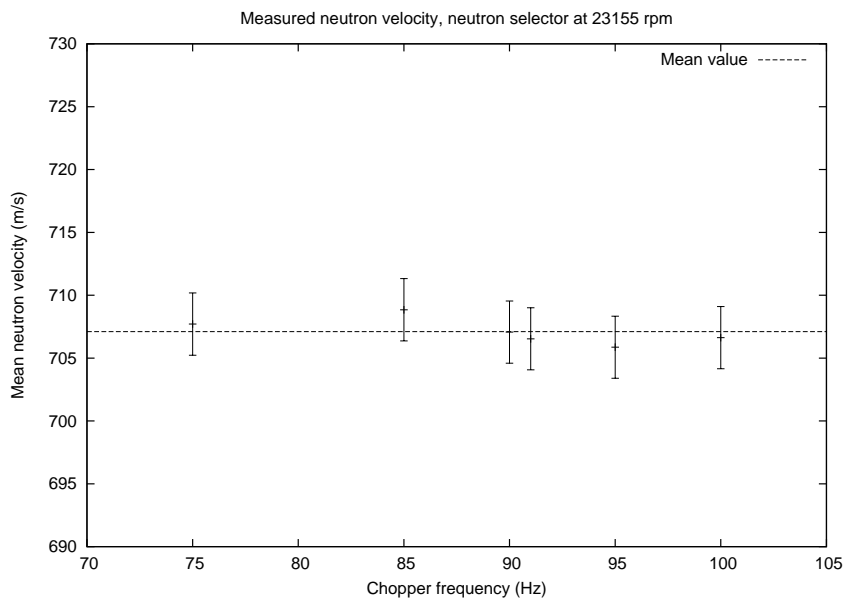


Figure 3.2: The mean neutron velocity is determined from the neutron time of flight between two aluminium foils inside the instrument. Two sodium iodide counters detect the spontaneous  $\gamma$  emission at the foils position. The distance between the foils is 2 m, velocity selector turns at 23155 rpm. The measurement yields a mean velocity of  $v = 707.1 \pm 0.4$  m/s. In addition to the error of the fit, we have a systematic error due to the uncertainty in the Al foil positioning of  $\pm 3$  m/s.

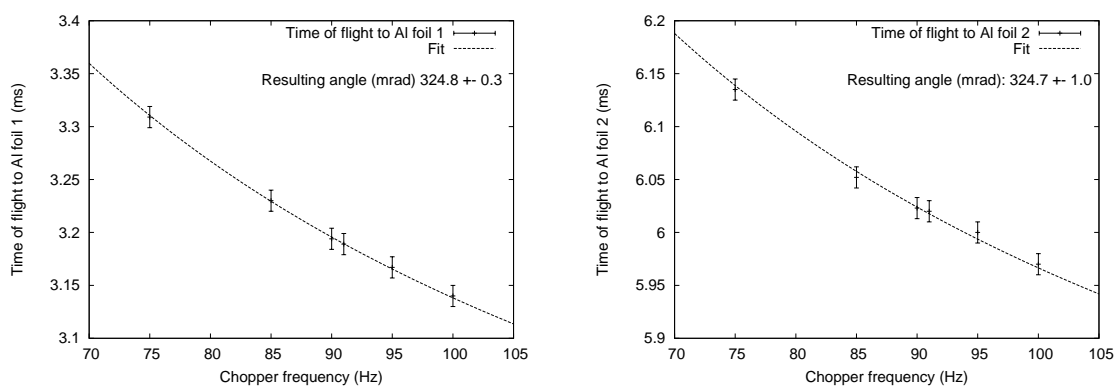


Figure 3.3: The time of flight measurement allows us to calculate the angle  $\alpha_{\text{off}}$  between the chopper signal and the position of maximum transmission. The fit yields for detector 1 (upstream)  $\alpha_{\text{off},1} = 18.61 \pm 0.02^\circ$  and for detector 2 (downstream)  $\alpha_{\text{off},2} = 18.60 \pm 0.06^\circ$ . Both values agree within the errors and the error is dominated by the accuracy of the Al foil positions.

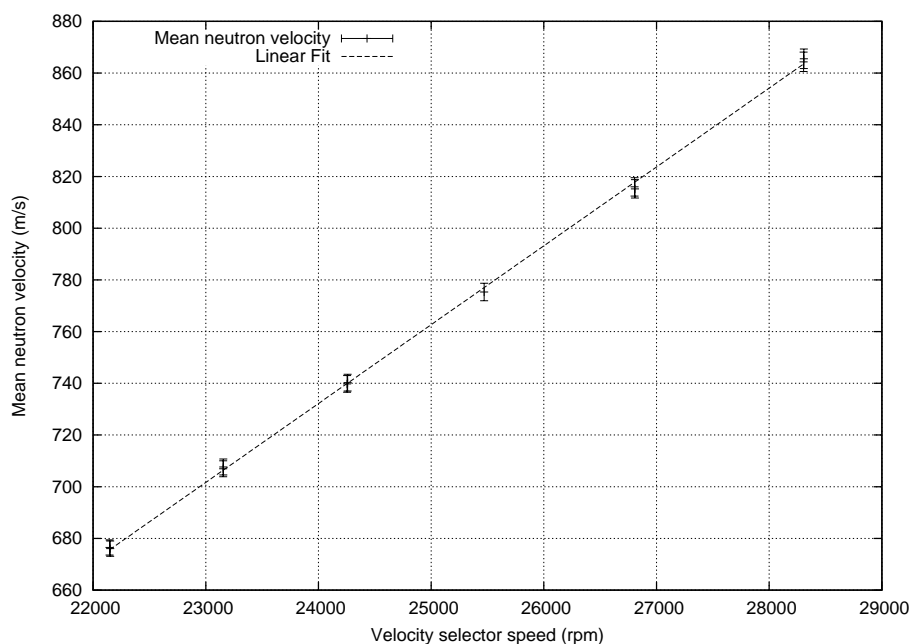


Figure 3.4: The neutron's mean velocity plotted against the frequency of the velocity selector. The linear relation is confirmed and the slope is  $30.51 \pm 0.016 \text{ m/s} \cdot (1000 \text{ rpm})^{-1}$ .

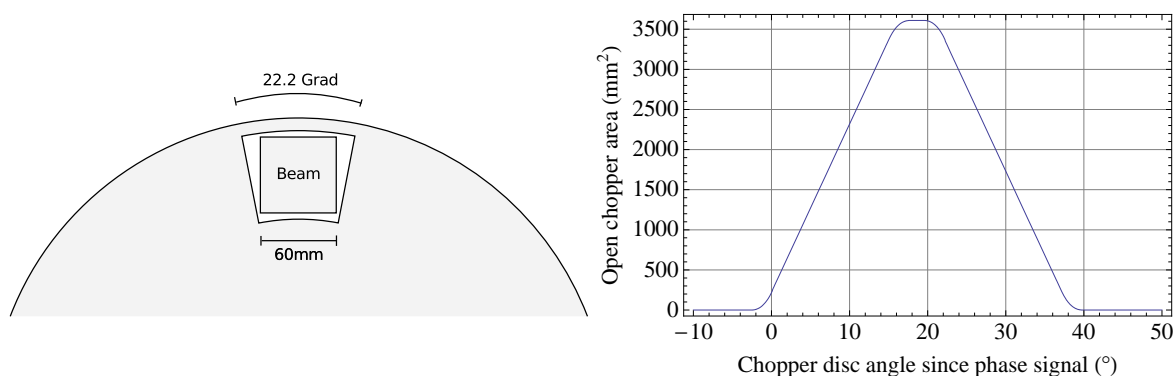


Figure 3.5: Left: The chopper geometry used for the calculation of the opening function. Rectangular beam profile results in a deviation from the triangular function. Right: The resulting chopper opening function.

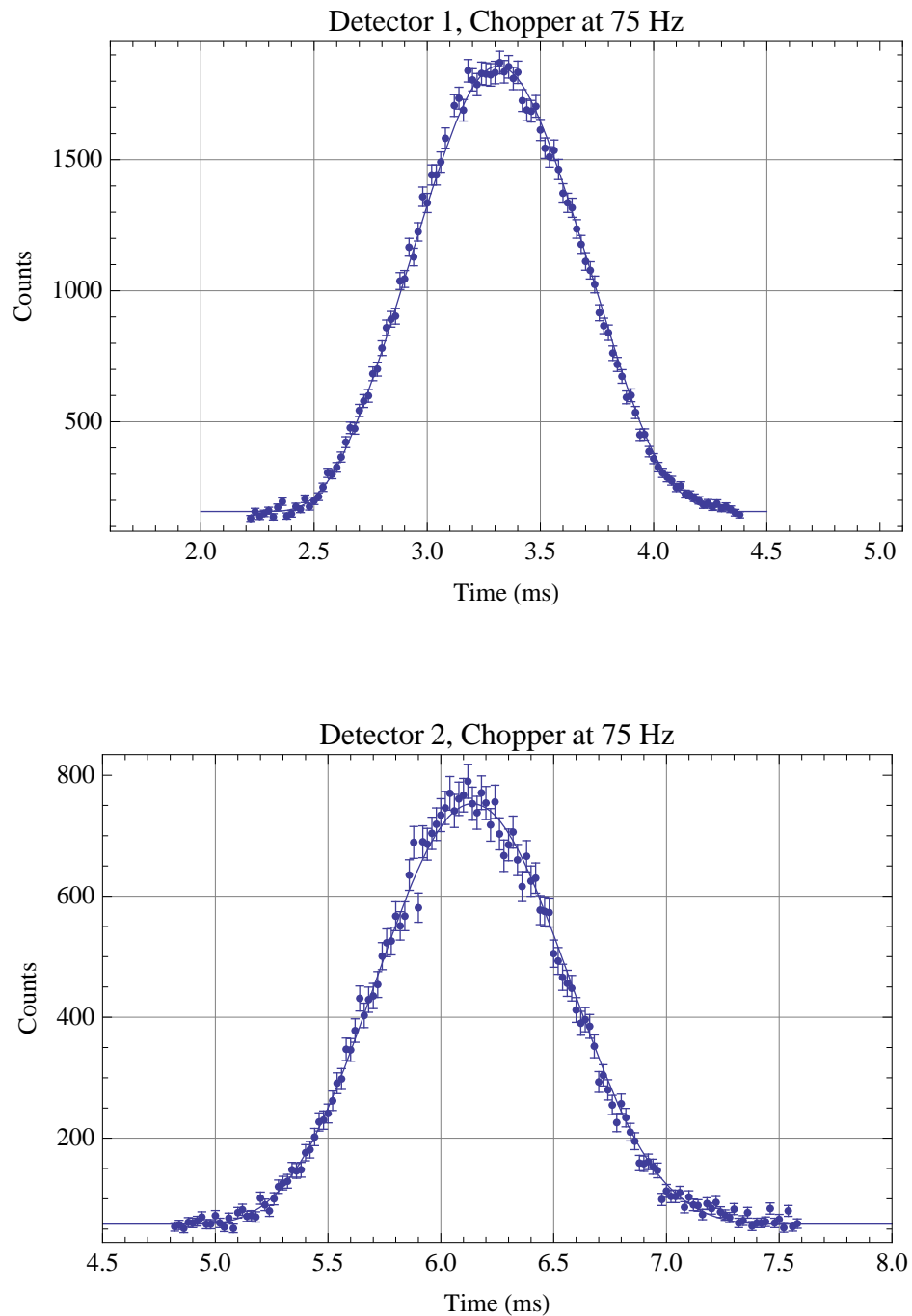


Figure 3.6: Fit of the predicted theoretical time dependent neutron flux densities at the positions of Al foil 1 and Al foil 2, indicated as  $d_{\text{begin}}$  and  $d_{\text{end}}$  in figure 1.1, respectively. The free parameters for the fit are the amplitude, a constant background offset and the FWHM of the neutron selector's velocity distribution. The time offset is fixed. Chopper is turning at 75 Hz and we use a mean neutron velocity of 707.1 m/s. All 108 data points are used for the fit. Also notable is the broadening of the pulse due to the velocity spectrum.

Detector	Chopper (Hz)	FWHM (%)	reduced $\chi^2$	
1	95	$12.0 \pm 1.7$	1.90	
	85	$12.2 \pm 2.4$	1.20	
	75	$11.5 \pm 2.6$	1.13	
2	95	$10.6 \pm 1.3$	1.19	
	85	$10.5 \pm 1.3$	1.70	detector saturated
	75	$10.0 \pm 1.6$	1.06	

Table 3.1: The FWHM of the velocity selector’s distribution estimated by a fit of the theoretical pulses to the measurement with the FWHM as a free parameter.

description of the chopper. The model of the chopper used in section 2.4 is well suited for calculating the disc’s geometry, but it does not take all the details of the aperture geometry into account as the beam is shaped by rectangular apertures while the chopper window is a circular sector for stability reasons.

In order to calculate the opening function with higher accuracy, we use the real beam profile shown in figure 3.5 and describe the opening with a piece-wise defined function. Using this chopper opening function and the velocity distribution of the neutron velocity selector, we can calculate the time dependent neutron flux at any cross section inside the instrument by integrating over the velocity spectrum, therefore calculating the convolution

$$\Phi_d(t) = \int_{v_1}^{v_2} dx A_{\text{open}} \left( 2\pi f \left( t - \frac{d}{v} \right) \right) \bar{v}(v) \quad (3.4)$$

where  $\Phi(t)$  is the time dependent neutron flux at the distance  $d$  from the chopper and  $\bar{v}(v)$  the neutron velocity distribution of the selector.  $\bar{v}(v)$  is assumed to be a triangular distribution with a FWHM of about 13% as shown in the velocity selector’s manual and in the measurement shown in [Mä06]. The change in selectivity for neutrons moving not parallel to the beam axis [Ros04] can be neglected. The geometry of the setup is well known, same as the neutron’s mean velocity and the offset between the chopper trigger signal and the position of maximum transmission. We therefore fit the opening function with the velocity selector’s width, the amplitude and a constant background offset as free parameters in order to see how sensitive we are to changes in the selector’s width and if we can confirm the figures given in the selector’s manual. Two examples of these fits are shown in figure 3.6. The predicted pulses agree very well with the measured data and table 3.1 lists the resulting values.

### 3.3 Neutron Background at the Chopper

Tritium nuclei, produced by the cold neutrons of the beam and the  ${}^6\text{Li}$ , create fast neutrons in several different interactions with lithium, fluor, carbon, oxygen and hydrogen contained in the absorber material or the surroundings of the chopper case. This background event rate should ideally be constant during one turn of the chopper disc and is expected to be reduced during the opening of the chopper. The variable rate during the chopper opening is of no concern to the measurement because

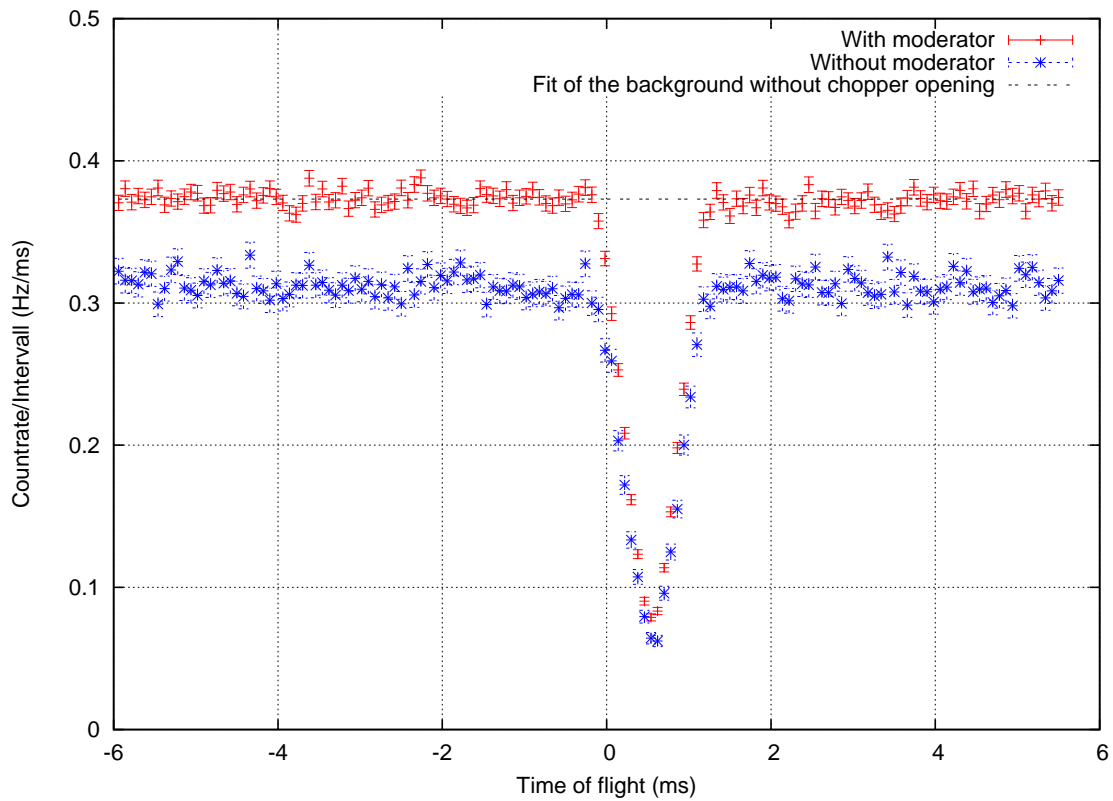


Figure 3.7: Neutron count rate measured as close as possible to the beam pipe at the chopper's location using a boron shielded neutron counter, with and without a neutron moderator inside the shielding. The moderator increases the detection probability of the fast neutrons that pass through the boron shielding. The two measured data sets are within the errors proportional to each other. Since we only increased the detection efficiency for fast neutrons between the two measurements, we conclude that the detector is, within the errors, sensitive to fast neutrons only.

no data is being taken during this time span. A variation of the event rate caused by inhomogeneities of the absorber material would be problematic since such a time dependent background could not be measured independently and would not be deductible. We therefore quantify the homogeneity of the chopper disc regarding the production of fast neutrons by using a helium counter. The detector is shielded by 1 cm of boron plastic. The absorption cross section of boron plastic is much larger for cold neutrons than for fast neutrons. The counter is placed in a distance of 20 cm to the chopper window on the downstream side of the chopper case below the beam line. In order to verify, that the detector is only sensitive to fast neutrons, a time of flight spectrum is measured both with and without a neutron moderator inside the shielding of the helium counter. Since the helium counter has a higher detection probability for cold neutrons, the moderator increases the probability of fast neutrons being detected. We expect both measurements to be proportional to each other if only fast neutrons get through the boron plastic shield. The result of this measurement is shown in figure 3.7. The time of flight histogram for the measurement with a neutron moderator can be fitted by a scaling factor  $a$  to the data taken without the moderator. The result is  $a = 1.196 \pm 0.033$  with a reduced  $\chi^2 = 1.076$  and 143 degrees of freedom. We conclude, that the detector is sensitive to fast neutrons only. To estimate the homogeneity of the neutron background, we fit a constant  $c$  to the data while excluding the data points during the chopper opening. The fit gives a mean value of  $c = 0.3731 \pm 0.0005$  Hz/ms with a reduced  $\chi^2 = 1.026$ . We conclude, that the background of fast neutrons produced by the chopper is therefore sufficiently constant for the measurement.

### 3.4 Neutron Background on Central Solenoid

As in section 3.3, we look for time dependent neutron background. The helium counter is placed at the joint of the first detector vessel and the central solenoid outside of the vacuum. Neutrons might scatter at the chopper or the apertures after the chopper and interact at the end face of the upstream detector vessel. We took a cumulative 118 hours of data with the helium counter. The time of flight histogram is shown in figure 3.8. The fit of a constant  $c$  for data points results in  $c = 4.941 \pm 0.001$  Hz/ms with a reduced  $\chi^2 = 1.17$ . While the statistic is still too low to draw a final conclusion, we can say that some structure is present. We particularly see structure around 5 ms which corresponds roughly with the position of the calibration device. More structure is visible during the beam stop peak at 7.8 ms and around 9.6 ms which might be caused by neutrons which are backscattered from the beam stop. Since we measured the time of flight spectrum in close vicinity to the chopper without seeing this structure, we conclude that this time dependence is not caused by the chopper itself. Despite that, we see that the variations during the signal measurement time span are on the order of  $2 \cdot 10^{-3}$  and will be considered during the final evaluation.

### 3.5 Verification of the Chopper Timing

We show that the measurement with the PERKEO III detectors can confirm the predicted chopper timing. In order to do that, we evaluated the time of flight data taken

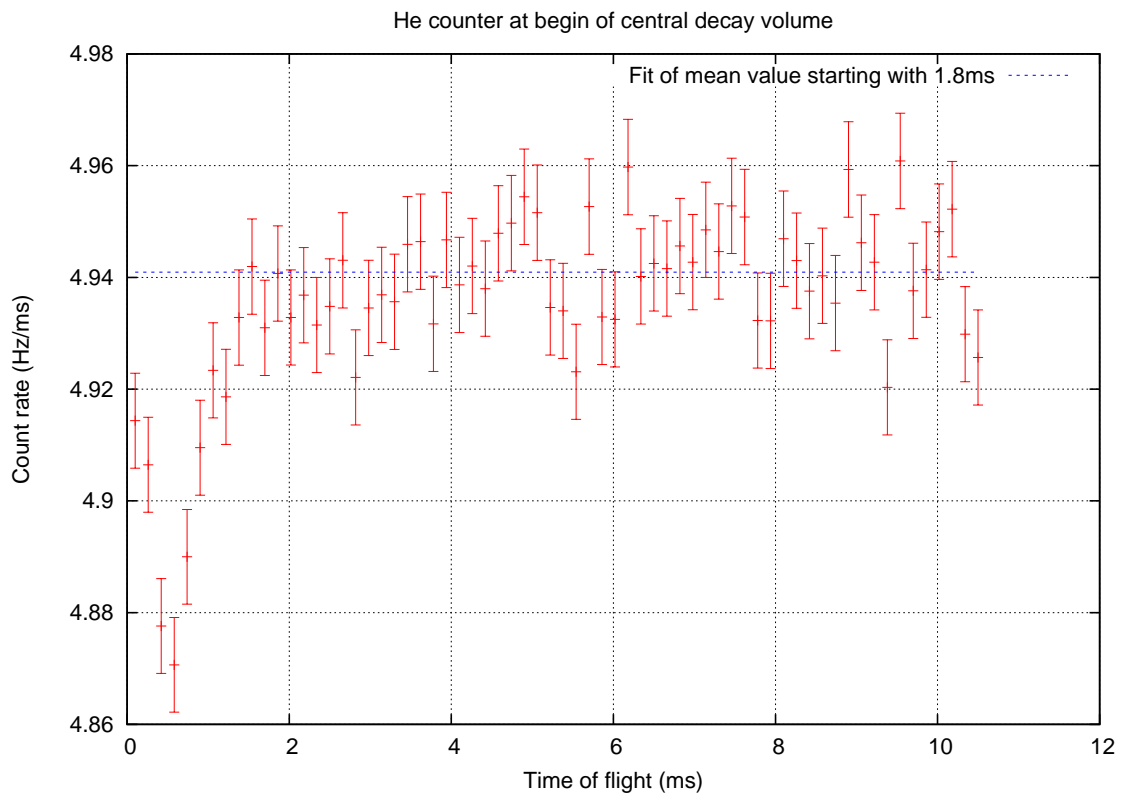


Figure 3.8: Time of flight data measured with a He neutron counter placed at the joint between the central beam tube and the upstream detector vessel, outside of the vacuum, in a distance of 50 cm to the beam. Data was taken from May 22nd until the 1st of June, yielding 118 hours of measurement time. The constant fits with  $c = 4.941 \pm 0.001$  Hz/ms.

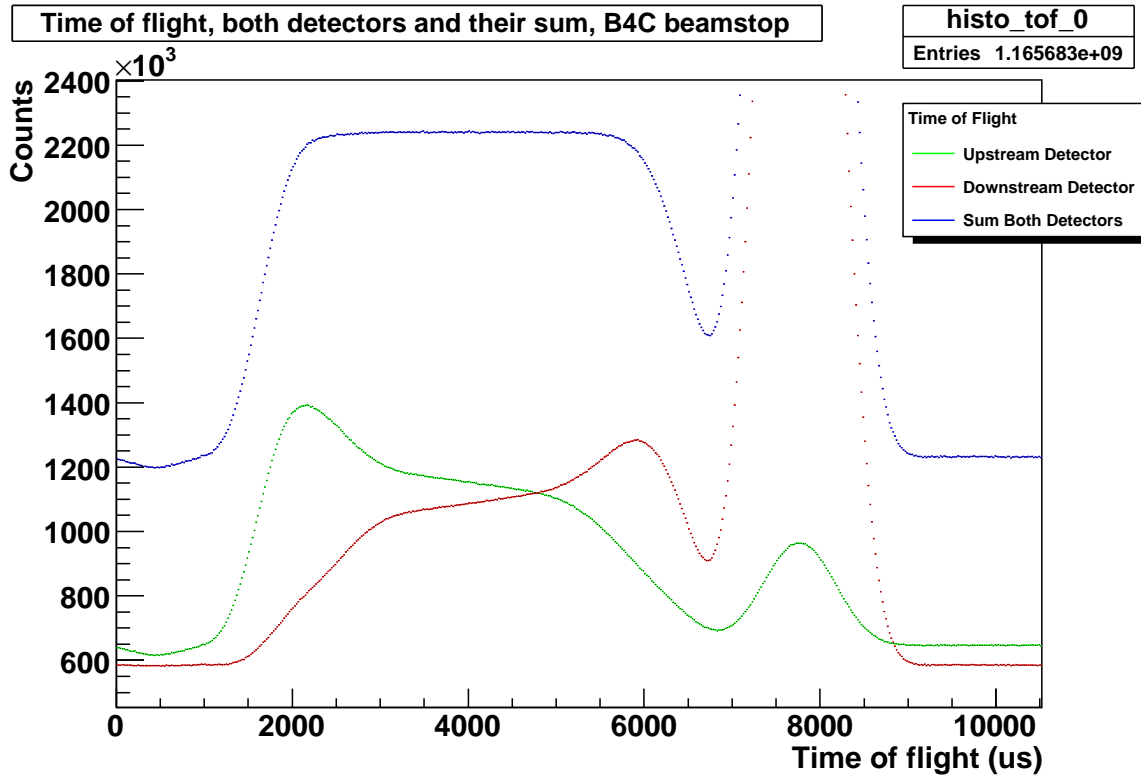


Figure 3.9: Time of flight histogram, measured with PERKEO III. Drawn here is the sum of both detectors, the upstream detector with the smaller peak at  $7800 \mu\text{s}$ , and the downstream detector. One can see the total background level of  $1.35 \cdot 10^6$  counts/bin, the increased event rate during the time between 2 ms and 6 ms due to the neutron decay electrons getting mapped onto the detectors, and the large peaks at 7.8 ms caused by the beam stop. One can also see the chopper opening at 0.5 ms in the upstream detector. The count rates of both individual detectors are not constant during the time span of the signal measurement between about 3.2 ms and 4.8 ms due to the expected magnetic mirror effect (Section 3.9). The sum is constant, which means that both detectors have comparable detection efficiencies. Data was taken from 06/01 until 06/17, the bin width is  $20 \mu\text{s}$  and the whole energy range is shown. Error bars are too small to be seen.

during the time from the 1st of June until the 17th of June with 94 Hz chopper frequency and a neutron wavelength of 5.0 Å, which corresponds to a mean velocity of 775 m/s. In the data shown in figure 3.9, one can see the chopper opening at  $480 \pm 50 \mu\text{s}$  in the slight decrease of the upstream detector's event rate, whereas the model predicts a maximum of the chopper transmission at  $520 \pm 12 \mu\text{s}$ . The plateau between 2.5 ms and 5.5 ms, where the total count rate of both detectors remains nearly constant, is the phase of the measurement during which all decay electrons are mapped on one of the two detectors. This time span of constant event rate is centered around  $4040 \pm 50 \mu\text{s}$  which agrees very well with the predicted  $4083 \mu\text{s}$  of the model. The maximum of the beam stop peak is located at  $7755 \pm 5 \mu\text{s}$  whereas the predicted value was  $7800 \pm 100 \mu\text{s}$ . The begin of the beam stop peak was predicted for  $6.8 \pm 0.1 \text{ ms}$  (measured  $6.7 \pm 0.2 \text{ ms}$ ) and the end was predicted at  $8.7 \pm 0.1 \text{ ms}$  (measured  $8.8 \pm 0.2 \text{ ms}$ ). The maximum of the beam stop peak position is determined more precisely since the maximum can be found more accurately.

The measured timing agrees very well within the errors with the predicted values and we therefore conclude, that our model of the chopper geometry and the calibration of both the velocity selector and the chopper's trigger signal is reliable.

### 3.6 $\gamma$ -Background from the Chopper

Neutrons reaching the  ${}^6\text{LiF}$  produce not only a background of fast neutrons, but also  $\gamma$ -radiation. We quantify this  $\gamma$  background from the chopper using a NaI counter directly on top of the chopper case in a distance of 10 cm to the chopper window and measure the time of flight spectrum of the  $\gamma$  background for different chopper frequencies. The count rate, as shown in figure 3.10, is during the chopper opening greatly reduced, as expected. Also, after the closing of the chopper window, one can see time dependent variations. The background depends on the chopper phase angle as shown in figure 3.10. These variations are caused by impurities in the absorber material or on the surface and the PERKEO III detectors were shielded with 15 cm Pb against this background.

### 3.7 Uncertainty in Background Measurement

The background is measured after the neutron packet has been absorbed by the beam stop. The neutron pulse produces instantaneous  $\gamma$  background on the beam stop, clearly visible in the time of flight histogram. There is also delayed background due to backscattered neutrons. We compare two different beam stops, one made of  ${}^6\text{LiF}$  and the other one made of  ${}^{10}\text{B}_4\text{C}$ . The ratio

$$\frac{\sigma_{\text{scatter}}}{\sigma_{\text{absorb}}} \quad (3.5)$$

of the cross sections for neutron scattering  $\sigma_{\text{scatter}}$  and neutron absorption  $\sigma_{\text{absorb}}$  is four times lower for  ${}^{10}\text{B}_4\text{C}$  than for  ${}^6\text{LiF}$ . Since all neutrons are either absorbed or scattered at the beam stop, the  ${}^{10}\text{B}_4\text{C}$  is better suited for our application.

The background, which is measured after the beam stop peak, will be used for subtracting the background from the signal, which is measured from approximately

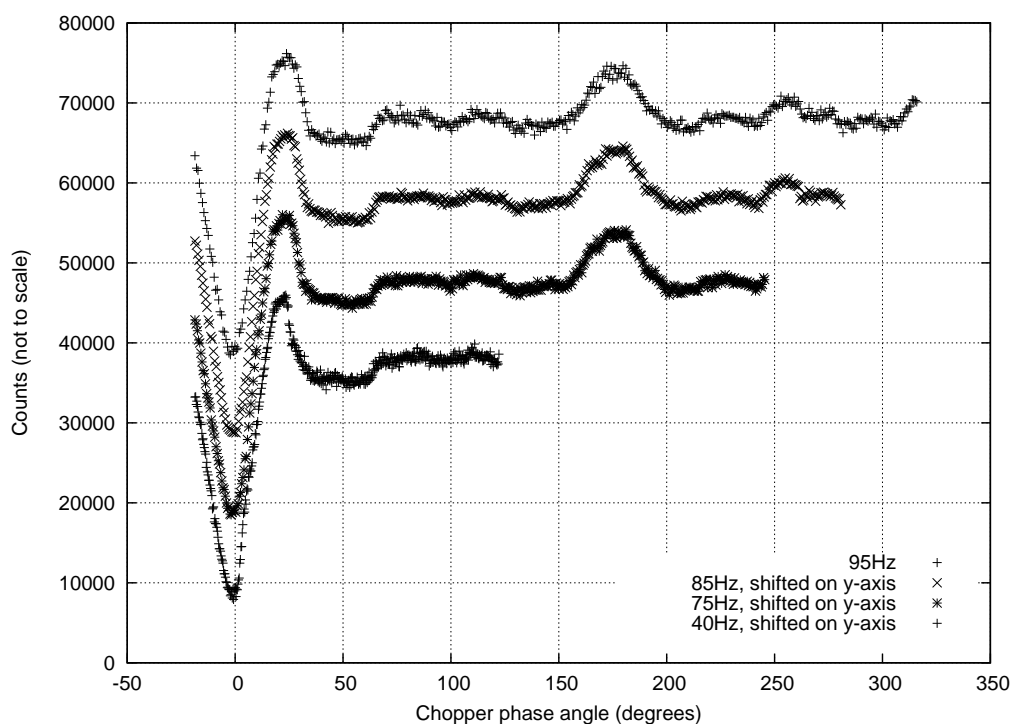


Figure 3.10: Time structure of the chopper measured with a  $\gamma$ -counter directly on top of the chopper case without shielding. The measurements were done with different chopper frequencies to distinguish photons created directly by the chopper and photons created by scattered neutrons. Since the data sets are proportional to each other, we conclude that the NaI counter sees only photons created directly on the chopper disc. The curves are plotted with a constant offset to separate them for printing.

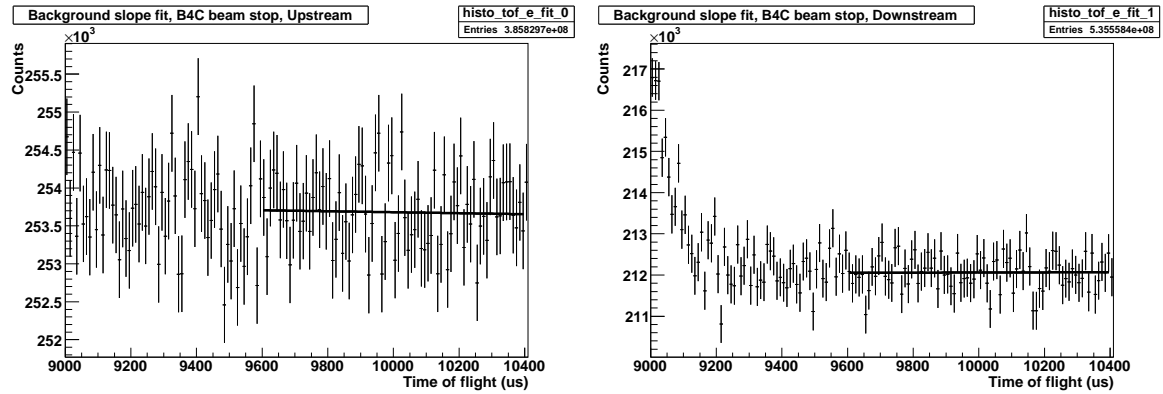


Figure 3.11: Time of flight histogram for the upstream (left) and downstream (right) detectors after the beam stop peak using the  $^{10}\text{B}_4\text{C}$  beam stop. Same data set as in figure 3.9, except that we only look at events in the energy range between 250 MeV and 650 MeV where the evaluation of the  $\beta$ -asymmetry measurement takes place. The downstream detector is affected by the beam stop peak for a much longer time than the upstream detector. While upstream could measure background beginning at 9.3 ms, the data of the downstream detector is not stable before 9.6 ms. The slopes are fitted with a linear function, resulting in a relative slope of  $-2.535 \pm 0.019 \cdot 10^{-4} \text{ ms}^{-1}$  for the upstream detector and  $-8.815 \pm 0.228 \cdot 10^{-5} \text{ ms}^{-1}$  for the downstream detector. Also compare a similar analysis using the  $^6\text{LiF}$  beam stop in figure 3.13.

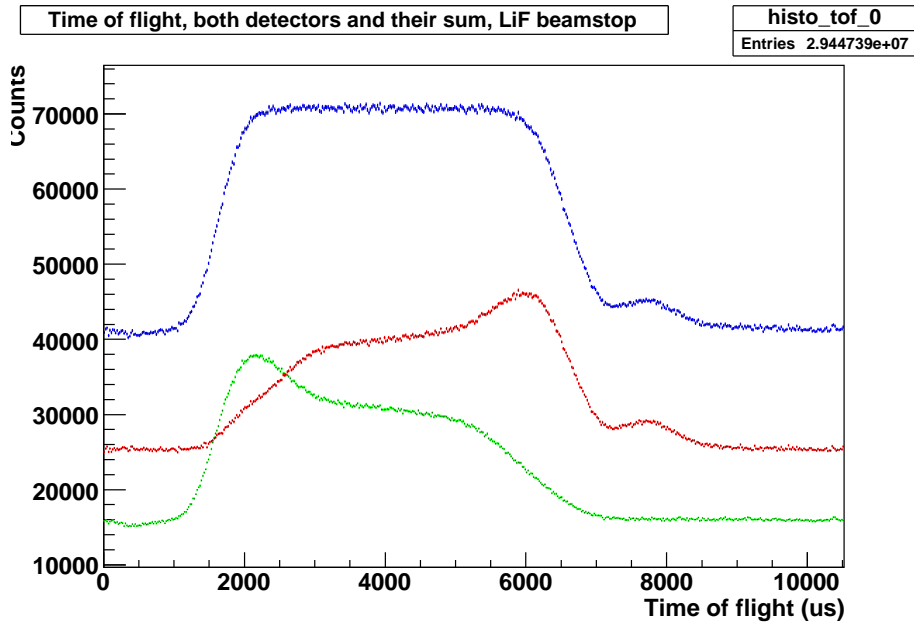


Figure 3.12: Time of flight histogram of the measurement using a  $^6\text{LiF}$  beam stop. Data was taken from the 18th to the 20th of April 2009. It is noticeable that the  $^6\text{LiF}$  beam stop produces a much smaller beam stop peak than  $^{10}\text{B}_4\text{C}$  since  $\gamma$ - production is suppressed by  $10^{-4}$ .

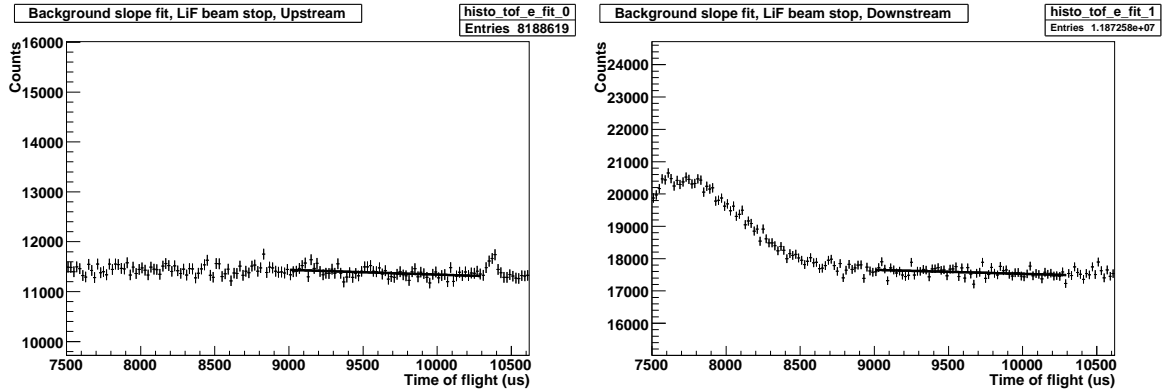


Figure 3.13: Time of flight histogram for the upstream (left) and downstream (right) detectors after the beam stop peak using the  ${}^6\text{LiF}$  beam stop. Same data as shown in figure 3.12, but only energies between 250 MeV and 650 MeV. As in the analysis of the  ${}^{10}\text{B}_4\text{C}$  beam stop (figure 3.11), we are fitting the background measurement time span using a linear function, resulting in a relative slope of  $-8.329 \pm 0.029 \cdot 10^{-3} \text{ ms}^{-1}$  for the upstream detector and  $-6.950 \pm 0.019 \cdot 10^{-3} \text{ ms}^{-1}$  for the downstream detector.

3.5 ms up to 4.5 ms. In the data of figure 3.11 we see a slight slope in the background. A possible explanation is backscattering of neutrons from the beam stop. We estimate the maximum correction on  $A$  by starting with

$$A = \frac{S^\uparrow - S^\downarrow}{S^\uparrow + S^\downarrow - B_m} \quad (3.6)$$

where  $S^\uparrow = N^\uparrow + \frac{1}{2}B_m$  and  $S^\downarrow = N^\downarrow + \frac{1}{2}B_m$  are the number of events measured for spin up and spin down, respectively, and  $B_m$  denotes the total number of background events during the measurement of the decay electrons. We assume that the background rate during signal measurement is the same as during the background measurement, so that

$$B_m = \frac{t_s}{t_b} B = \alpha B \quad (3.7)$$

is proportional to the ratio of the signal measurement time span  $t_s$  and the background measurement time span  $t_b$ . Assuming that the true background has a deviation from the mean value of

$$\Delta B = \frac{1}{2}(B_{\max} - B_{\min}) \quad (3.8)$$

where  $B_{\max}$  and  $B_{\min}$  are the measured maximum and minimum counts, we see that the maximum correction to the measured asymmetry due to the uncertain background amounts to

$$\frac{\Delta A}{A} \leq \frac{\alpha \Delta B}{S^\uparrow + S^\downarrow - \alpha B} \quad (3.9)$$

Using the estimated slopes on the background of the two detectors, we can estimate  $B_{\max}$  and  $B_{\min}$  by the highest and lowest values of the straight line fit and calculate the maximum corrections for the two detectors:

B <sub>4</sub> C beam stop		
	Detector 1	Detector 2
B	$2.030 \cdot 10^7$	$1.696 \cdot 10^7$
$\Delta B$	$2.058 \cdot 10^3$	$5.981 \cdot 10^2$
$\alpha$	1.25	1.25
$S^\uparrow + S^\downarrow$	$4.343 \cdot 10^7$	$3.919 \cdot 10^7$
$\Delta A/A$	$7.1 \cdot 10^{-5}$	$2.1 \cdot 10^{-5}$

As a comparison, we also analyze in the same manner the time of flight data taken with a <sup>6</sup>LiF beam stop installed. The data set is much smaller since we replaced the LiF beam stop by B<sub>4</sub>C soon.

LiF beam stop		
	Detector 1	Detector 2
B	$7.434 \cdot 10^5$	$1.147 \cdot 10^6$
$\Delta B$	$3.998 \cdot 10^3$	$5.168 \cdot 10^3$
$\alpha$	0.77	0.77
$S^\uparrow + S^\downarrow$	$1.039 \cdot 10^6$	$1.391 \cdot 10^6$
$\Delta A/A$	$3.3 \cdot 10^{-3}$	$3.9 \cdot 10^{-3}$

We can see from this analysis, that the correction due to the slope on the background signal created by the beam stop is much higher for the <sup>6</sup>LiF beam stop than for the <sup>10</sup>B<sub>4</sub>C beam stop. The <sup>6</sup>LiF produces far less instantaneous  $\gamma$  background, but it also has a higher probability for backscattering of cold neutrons, which in turn increases the variations in the background signal after the beam stop. This analysis shows, that using the <sup>10</sup>B<sub>4</sub>C beam stop, the limits for the necessary correction of the background measurement will be on the order of  $10^{-4}$ . The detailed calculation of this correction during the final evaluation of the  $A$  measurement will also take the thermal drifts of the detectors and electronics into account, as well as the detector function and the long time behavior of the scintillators.

### 3.8 High Energy Background

As another systematic check, we look at events with a total energy of at least 1050 keV, which is about 1.3 times the maximum expected energy of the  $\beta$ -decay electrons. We conduct this high energy cut well above the maximum  $e^-$  energy because the Poisson statistic of the photomultipliers' amplification stages broadens the spectrum by about 30%. Otherwise, we would see the time of flight signature of the decay electrons which get mapped onto the detectors as shown in figure 3.9. In this analysis, we're interested in evidence for neutrons hitting the vacuum vessel of the instrument.

We evaluate the PERKEO III data of 1st of June until the 17th of June, a time span of almost continuous operation. The detectors are calibrated at least twice a day with several radioactive isotopes, and the detector drifts due to changes in temperature are controlled by multiple small calibration measurements with a single source (Sn).

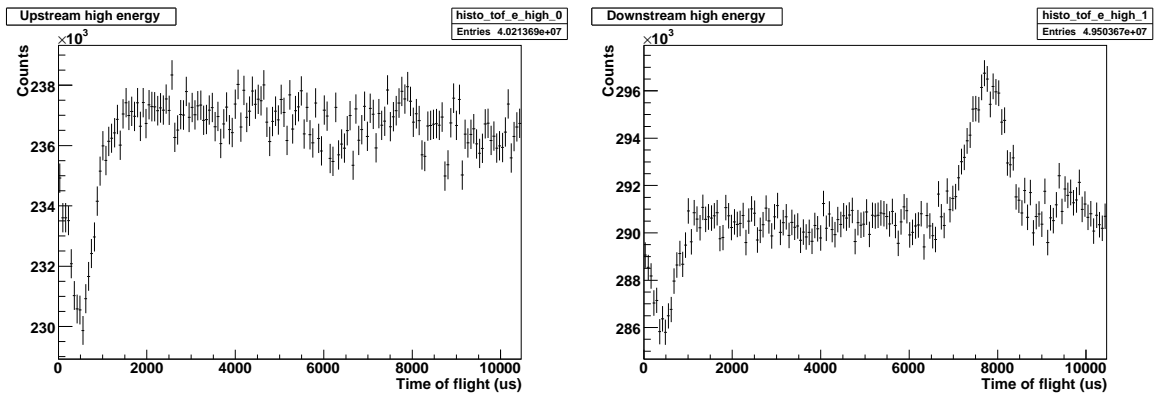


Figure 3.14: Time of flight histograms of events with more than 1050 keV, re-binned by a factor of 120, using a  $^{10}\text{B}_4\text{C}$  beam stop. One can see the opening of the chopper at 500  $\mu\text{s}$  as a decrease in event rate by 2.9% in the upstream detector above the chopper, and by 1.5% in the downstream detector above the beam stop. Since the change in event rate is instantaneous, what we see here is the change in production of  $\gamma$  and fast neutrons at the chopper surface as the radiated area changes during the opening. At 7800  $\mu\text{s}$ , one can see events produced at the beam stop. While this peak is clearly visible in the downstream detector, it is much smaller in the upstream detector because of the small solid angle. Also, at 9600  $\mu\text{s}$ , there is another peak visible in the downstream detector which is probably caused by neutrons backscattered from the beam stop. The duration between the beam stop peak and this additional peak is approximately 1800  $\mu\text{s}$ , corresponding to 1.4 m flight distance.

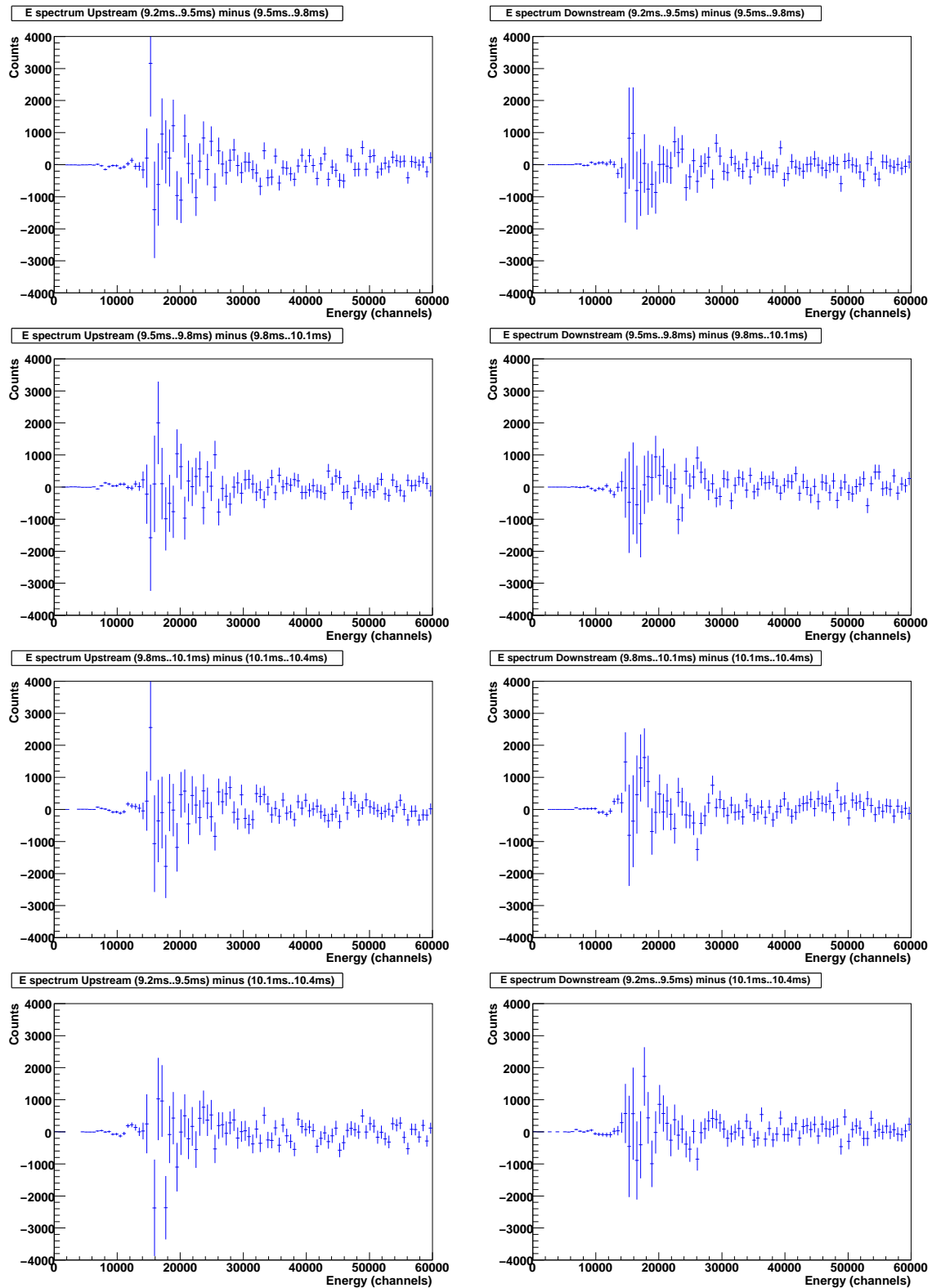


Figure 3.15: The time span of the background measurement from 9.2 ms to 10.4 ms is divided into 4 equal parts. The histograms show the differences in the background energy spectra for consecutive time spans, as well as the differences between the first and the last time span. We see, that the differences are almost compatible with zero, as expected. The data was taken from 06/01 until 06/17 using the  $^{10}\text{B}_4\text{C}$  beam stop.

The calibration samples are listed in table 3.2. From this calibration, we find for the cutoff energy 1050 keV the energy channels 40380 and 43090 for the upstream and downstream detectors, respectively.

Sample		Mean peak energy (keV)
Cerium	$^{139}\text{Ce}$	136.6
Tin	$^{113}\text{Sn}$	371.9
Cesium	$^{134}\text{Cs}$	629.3
Bismuth	$^{207}\text{Bi}$	504.5
	$^{207}\text{Bi}$	996.9

Table 3.2: Calibration samples [Rei99].

neutrons have a mean velocity of 775 m/s. This corresponds to a distance of 1.40 m, which matches the distance between the beam stop and the joint between the downstream detector vessel and the central tube.

As another test, we take the energy spectra for different time spans of equal length during the background measurement and inspect the differences in their energy spectra. We don't expect to see a structure here, which would indicate a new background effect. Figure 3.15 shows the differences between the spectrum of one time span and the following. The differences are very small, mostly compatible with zero, and there is no distinctive signature visible.

The corresponding time of flight histograms for these high energy events are shown in figure 3.14. One very interesting feature is the additional peak after the beam stop at around 9600  $\mu\text{s}$ , caused by neutrons backscattered from the beam stop. The time between the beam stop peak and this additional peak is approximately 1800  $\mu\text{s}$ . With the selected wavelength of 5.0  $\text{\AA}$  the neu-

### 3.9 Magnetic Mirror Effect

Decay electrons, on their way to one of the detectors, can be reflected by the magnetic mirror effect caused by an inhomogeneous magnetic field. We briefly discuss this effect and show the optimizations done to the magnetic field of PERKEO III.

In an inhomogeneous magnetic field, charged particles with an angle  $\theta$  between their momentum and the magnetic field, which is greater than a critical angle  $\theta_c$ , can be reflected. The critical angle is given by

$$\sin \theta_c = \sqrt{\frac{B_0}{B_{\max}}} \quad (3.10)$$

where  $B_0$  is the magnetic field strength at the point where the decay electron was created, and  $B_{\max}$  the maximum magnetic field that the electron will encounter.

PERKEO III measures the decay electrons integrated over the hemispheres in both the direction of the neutron spin and against it. An inhomogeneous magnetic field causes electrons to be mapped on the wrong detector due to the magnetic mirror effect. The experimental asymmetry

$$A_{\text{exp}}(E) = \frac{N^\uparrow(E) - N^\downarrow(E)}{N^\uparrow(E) + N^\downarrow(E)} \quad (3.11)$$

becomes distorted:

$$N_i(E) = \int_0^{\theta_c(B)} 2\pi \sin \theta \left(1 + (-1)^i \frac{v}{c} A \cos \theta\right) d\theta, \quad i = 1, 2. \quad (3.12)$$

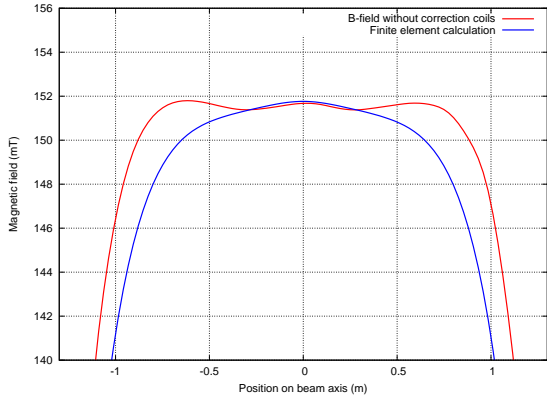


Figure 3.16: Measured magnetic field without correction coils and a theoretical prediction calculated by finite element simulation. The discrepancy is under investigation.

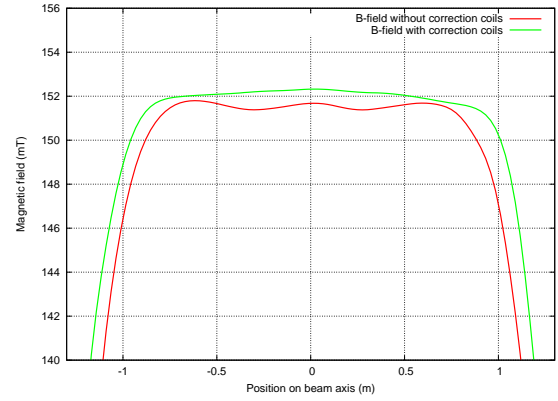


Figure 3.17: Comparison of the magnetic field before and after additional correction coils were mounted at the positions listed in table 3.3. The corrected field is free of local minima and the length of the homogeneous region is increased to 1.95 m.

with  $N_1 = N^\dagger$  and  $N_2 = N^\downarrow$ . For a point-like decay electron source, the magnetic mirror effect has a large influence on  $A_{\text{exp}}$  even for small changes in the magnetic field. This effect is greatly reduced when we go from the point-like particle source to a macroscopic source, like a cloud of neutrons. Calculation reveals [Rav95]

$$A_{\text{exp}} = \beta A \frac{M}{1 - k^2} \quad (3.13)$$

where  $M(\rho, B)$  and  $k(\rho, B)$  are functions of the neutron density distribution  $\rho(\vec{x}, t)$  and the magnetic field  $B(\vec{x})$ :

$$\begin{aligned} n_0 &= \int \rho(\vec{x}, t) d^3x \\ M &= \frac{1}{n_0} \int \rho(\vec{x}, t) \sin^2 \theta_c(B(\vec{x})) d^3x \\ k &= \frac{1}{n_0} \int \rho(\vec{x}, t) \cos \theta_c(B(\vec{x})) d^3x \end{aligned} \quad (3.14)$$

If the distribution  $\rho(\vec{x}, t)$  is symmetric to the maximum of the field  $B_{\text{max}}$ , the factor  $k$  vanishes. This property was used in [Mun06], where the total relative correction on  $A$  was only  $1.1 \cdot 10^{-3}$ .

### 3.10 B-Field Optimization

The magnetic field of PERKEO III was measured with a Hall effect probe along the beam axis. Figure 3.16 shows the measured field together with the values from a FEM simulation [Mä]. Measurement and predictions do not match very well. Especially the two local minima can not be explained by FEM simulation and would result

Position No.	Distance from center of the instrument (mm)	With (+) or against (-) the PERKEO III field	Windings	Current (A)
3	$\pm 267$	+	5	55
4	$\pm 374$	+	11	55
8	$\pm 801$	-	30	16
11	$\pm 1121$	+	30	55

Table 3.3: Positions and sizes of the correction coils.

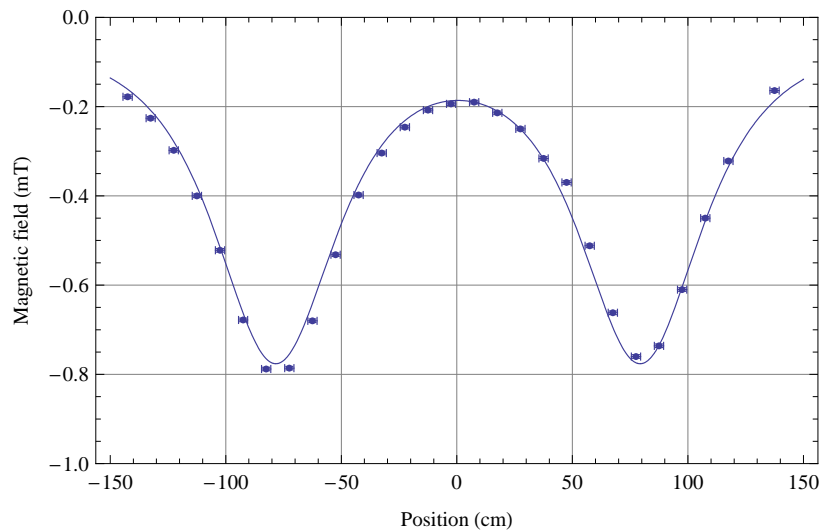


Figure 3.18: Predicted and measured field of the correction coils at position  $\pm 8$  (table 3.3). The largest error is the uncertainty in the  $z$ -position of the hall probe.

in magnetic bottles for charged particles. The reason for this discrepancy is under investigation.

The achievable event rate depends strongly on the usable length of the homogeneous magnetic field, defined by the points where the field drops below 98% of  $B_{\max}$ .

Additional correction coils are added to improve the homogeneity of the magnetic field. The field of the correction coils was measured and compared with the theoretical predictions. Figure 3.18 shows this measurement for the correction coil at position  $\pm 8$  (table 3.3). This measurement confirms that the theoretical description of our correction coils is sufficient and that we're able to search for an optimal configuration with numerical calculations. The positions of the correction coils can't be arbitrarily chosen because of the connectors for the water cooling system. On the outermost positions there are already correction coils installed. We search the parameter space for possible configurations, which create a magnetic field without minima even for a tolerance of  $\pm 1$  in the number of windings. From the possible configurations, we've chosen the one which reliably results in a homogeneous field of maximum length. The chosen configuration is summarized in table 3.3. Now, the outer correction coils increase the field strength in order to extend the usable decay volume, while the inner

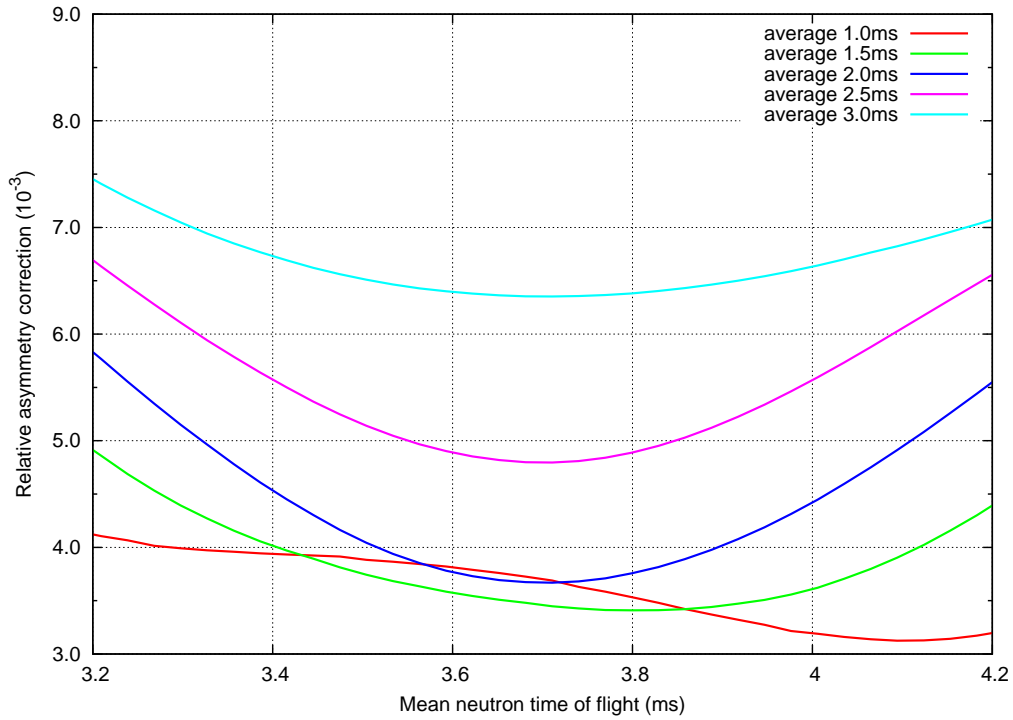


Figure 3.19: Relative corrections on  $A$  due to the magnetic mirror effect. The values were obtained using Monte Carlo simulation for a chopper frequency of 83 Hz, a neutron wavelength of  $5.0 \text{ \AA}$  and the magnetic field as measured as part of this thesis. The resulting corrections are on the order of  $5 \cdot 10^{-3}$ . Errors due to the uncertainties in the neutron time of flight are on the order of  $5 \cdot 10^{-4}$ . These are preliminary results and do not yet incorporate all known effects. Simulation program courtesy of Wang Xiangzun [Wan].

coils at positions  $\pm 3$ ,  $\pm 4$  and  $\pm 8$  remove the local minima. Figure 3.17 shows the optimized magnetic field. The field is now free of local minima and the usable length is longer than before.

### 3.11 Effect on the $\beta$ -Asymmetry

The measured values of the optimized magnetic field can now be used in a preliminary calculation to estimate the necessary corrections on  $A$ . The setup was simulated using a Monte Carlo method (Figure 3.19) and takes into account the actually realized setup. Shown here are the correction factors for different integration times as a function of the mean neutron time of flight. The corrections are on the order of  $3 \cdot 10^{-3}$ . Errors due to uncertainties in the time of flight offset are smaller than  $10^{-4}$  and therefore negligible. The estimates given here are preliminary results and a full field scan is scheduled after this beam time.



# Chapter 4

## Conclusion

For the 2008/2009 measurement with PERKEO III, a new low-background chopper system and the corresponding regulation electronics have been designed with the aim to reduce and analyze systematic effects of the instrument. The chopper was characterized with several time of flight measurements, and the predicted chopper opening function, neutron pulse shape and performance were confirmed. The chopper system reliably produced a pulsed beam with a high accuracy. The FWHM of the rotary frequency is  $2 \cdot 10^{-4}$  relative.

The background generated by the pulsed beam both at the chopper disc and at the beam stop has been analyzed using  $\gamma$ -, neutron- and electron-detectors. It was shown, that the  $\gamma$ -background created by the neutron beam on the chopper disc can be shielded and that the production of fast neutrons is constant in time within the errors. The effect of neutron backscattering at the beam stop and the implications for the background measurement have been analyzed. Two different beam stop materials ( $^{10}\text{B}_4\text{C}$  and  $^6\text{LiF}$ ) were compared and it was found that  $^{10}\text{B}_4\text{C}$  is better suited for our application due to the lower neutron backscattering probability.

The correction on  $\beta$ -asymmetry correlation coefficient  $A$  due to uncertainties in the background was estimated to be on the order of  $10^{-4}$  and will not limit the precision of the measurement. Moreover, the pulsed beam allowed a measurement of the magnetic mirror effect as a function of the neutron time of flight and the necessary correction due to this effect can therefore be optimized during data evaluation. This correction was estimated to be on the order of  $6 \cdot 10^{-3}$  and gives a systematic error of  $4 \cdot 10^{-4}$ . These estimates are still preliminary results and the final evaluation is ongoing.

From this analysis, low errors due to background related corrections are expected and we look forward to the evaluation of the asymmetry parameter  $A$  after this beam time. Figure 4.1 shows an example of a  $\beta$ -spectrum containing just one day of data.

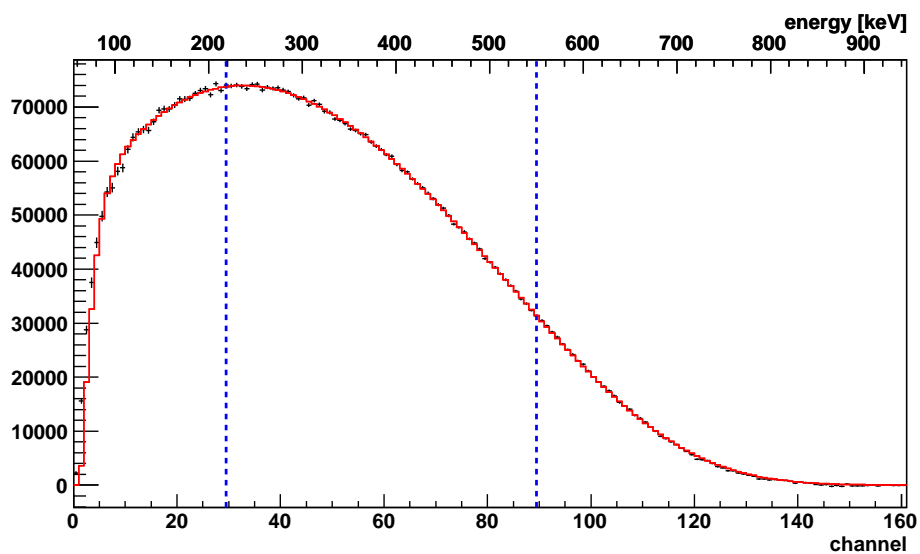


Figure 4.1: Histogram showing the differences of the energy spectra during the signal and background measuring time span. The fit function (red line) incorporates the detector triggerfunction, statistics of the photomultipliers and effects of the electronics. Shown here is one day of statistics. The detector calibration is not yet fully evaluated, so we don't account for thermal drifts and the position dependency of the detectors.

# Appendix A

## Additional Information

### A.1 LiF Tiles

$^6\text{LiF}$  is used in its polycrystalline form for the chopper coating. We discuss the improvements found regarding the production process. The method of choice is to first produce  $10\text{ cm} \times 10\text{ cm}$  big tiles by sintering the LiF powder and give them their final shape on the milling cutter as shown in figure 2.3. The raw tiles need to be inspected very carefully for hairline cracks and distortion which could let them crack during operation.

To prepare the  $^6\text{LiF}$  powder, we select material from old apertures and grind the material with a ball mill made of  $\text{AlO}_3$ . It is unknown how often and by which methods this material was processed before and due to the short supply of  $^6\text{LiF}$  and the large amount of discard especially at the beginning, when the process was not yet optimized, it was not possible to sinter all tiles in one batch from a homogeneously mixed powder.

To prepare a raw tile, 90 g LiF powder is poured into a metal frame and pressed at 12 bar for 2 minutes. Lithium fluoride is very aggressive, especially during sintering at temperatures as high as  $720^\circ\text{C}$ . The material must therefore have no contact with the frame during sintering. To protect the LiF we put a sheet of  $\text{AlO}_3$  underneath and remove the frame after pressing. This procedure is very delicate since the pressed raw tiles are very fragile and susceptible to hairline cracks which let them break during sintering. A new set of tools was produced in order to optimize this procedure. The frame can now be removed more safely than before and the more massive base plates reduce the risk of the tiles breaking in the oven due to the deformation of the base plates when heated.

During sintering, one can regulate the degree of fusion with the temperature and the duration of the process. Higher temperature results in a higher degree of fusion and therefore in more stable tiles, but at the same time increases the size of the formed crystals. It was therefore necessary to further optimize this process to produce tiles with less macroscopic crystals than the tiles of previous experiments but with a sufficient rigidity that prevents them from breaking during chopper operation. We found a good trade-off between crystals and unstable tiles by increasing the temperature slowly over a period of 240 minutes up to  $720^\circ\text{C}$  and keeping this temperature for another 120 minutes. The tiles were then allowed to cool slowly for 12 hours to a temperature of  $200^\circ\text{C}$  before the oven was slightly opened. The tiles have now a

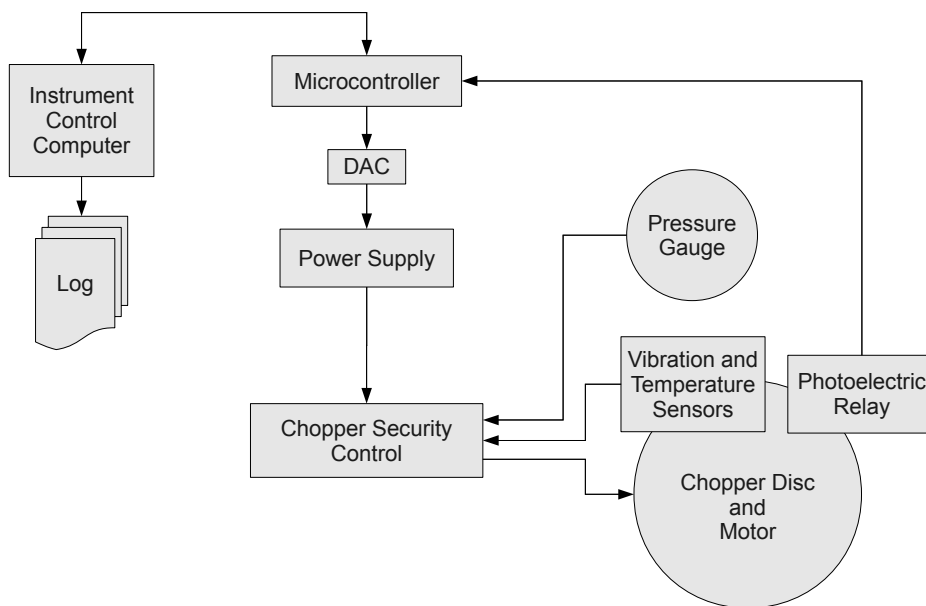


Figure A.1: Overview of the components of the chopper system.

much more homogeneous and more white appearance than before which indicates the reduction of macroscopic crystals. Contrary to previous experiments, we found that it is not necessary to cover the raw tiles with another layer of  $\text{AlO}_3$  and a metal plate, since the very slow increase of temperature leads to a homogeneous distribution of the heat. Also, during sintering, the tiles shrink by up to 10%. Another layer on top of the tiles interferes with this deformation and causes a larger amount of discard. Due to these optimizations, about 88% of the produced tiles were suitable for the chopper while virtually all could be very well used in other applications like normal apertures.

To mount the tiles later on the disc, they had to be shaped to a precision of 0.5 mm. This could be achieved by using the milling cutter of the fine mechanical workshop in Heidelberg. We produced special fittings in order to mount the tiles as strainless as possible and well cushioned onto the controlled machines where they could be processed under justifiable wearing of tools.

For the bonding of the tiles on the disc several two component glues have been tested. The combination of AW 116 resin and HV 953 U hardener proved the best choice regarding texture, resistance to shock and adhesion to LiF and the laminated fabric of the disc's base plate. The glue is prepared under vacuum by mixing resin and hardener at 0.1 bar to avoid the formation of air bubbles inside the glue matrix. The tiles are glued on the disc with their base area and their inner and outer radii. Special care is needed to avoid glue between the tiles' joints.

## A.2 Chopper Components

We describe the individual parts of the chopper system and give instructions and further references. Figure A.1 shows a schematic. The chopper system consists of the following components:

- **Chopper Disc:** The Chopper disc is mounted on the motor axis using a dowel. Care should be taken when removing the dowel to not widen the boring.
- **Power Supply:** The power supply must handle 160 W with a maximum current of 10 A and a maximum voltage of 26 V. The regulator is tuned for a power supply which accepts a control voltage in the range between 0 V and 5 V. The power for the motor is to be routed through the chopper security box, see the attached schematics.
- **Pickup Signals:** The chopper case features two pickup signals using photoelectric relays. The first pickup generates 60 pulses per second and is fed into the regulator. The second one is used as the phase signal for the measurement and as an additional cross check in the chopper security control box. A nice improvement would be to add a small amplifier directly on the chopper side, since we saw some crosstalk while running other electrical equipment near the signal path.
- **Security Sensors:** The chopper has two vibration sensors which are mounted near the vacuum feed-through and the motor itself. Both were glued directly on the vacuum case. There are also two K-type temperature sensors which should monitor the temperatures close to the vacuum feed-through and the motor. These four sensors and the second chopper pickup signal are connected to the respective connectors on the back side of the chopper security control box.
- **Security Control Box:** The security control box contains five instruments for the two vibration sensors, two temperature sensors, and one frequency sensor. Also, an external pressure gauge is connected to the system, since the motor can keep the nominal frequency of 100 Hz (a velocity on the outer radius of the disc of 520 km/h) only under vacuum. A relay switches the current for the chopper motor. The relay switches off, if any of the instruments' relays falls off. This mechanism can be overridden by the "Acknowledge" and "Stop" buttons on the front panel. While holding down the "Acknowledge" button, the main relay will be switched on regardless of the state of the instruments, while the "Stop" button will switch the main relay off. The main relay never switches on by itself, even when there is no fault condition. This avoids an automatic restart after a fault condition. This behavior can be easily changed if desired.
- **Regulator:** The regulator has connectors for the chopper pickup signal and an output of the control voltage for the power supply on the back side. There are also two USB connectors on the front side, the right one is for the connection with the PC. The left one supplies the regulator's DAC with 5V, since the regulator and the DAC are galvanically isolated.

- **Software:** The software part consists of the firmware for the regulator, a daemon on the PC side, which handles the communication with the controller and writes the log files, and a client program, which can be used to set the chopper's frequency and monitor the chopper's status. The daemon and the client program communicate via UDP, so one can easily control the chopper remotely. The firmware can be updated using a standard Atmel in-system programmer (ISP). There is a dedicated ISP mounted in the regulator box. The whole software and documentation files are contained in a source code repository on the computers of the PERKEO III group. The README file contained in the repository is a very good starting point regarding the chopper software components.
- **Regulation Parameters:** The coefficients for the integral and proportional regulator can be easily changed, if this should be needed. In order to not overload the motor, there is a step-wise linear calibration curve implemented in the controller. Please refer to the README file for instructions on how to change these settings.
- **Other Considerations:** After dismounting the chopper disc, make sure that the disc is still well balanced and connected securely to the motor axis before starting the chopper. Do not run the chopper with the case opened and make sure that it is not possible to reach into the chopper case with the rotating disc.

### A.3 Frequency Regulator

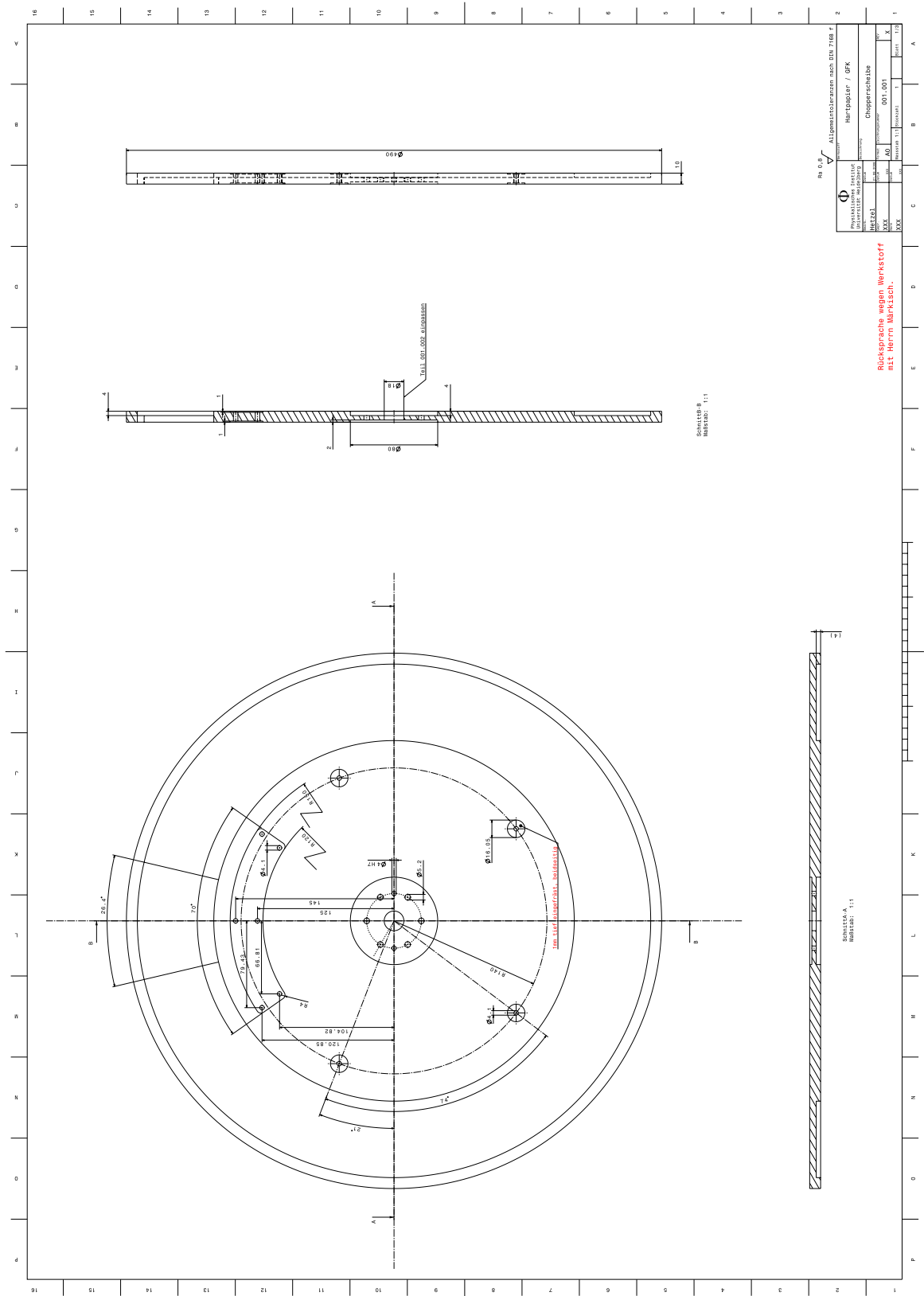
The frequency regulation must be able to keep the chopper's frequency stable for the whole beam time so that the time of flight diagrams consisting of the sum of all pulses are as precise as possible. The design goal for the regulator's relative precision is at least  $5 \cdot 10^{-4}$ .

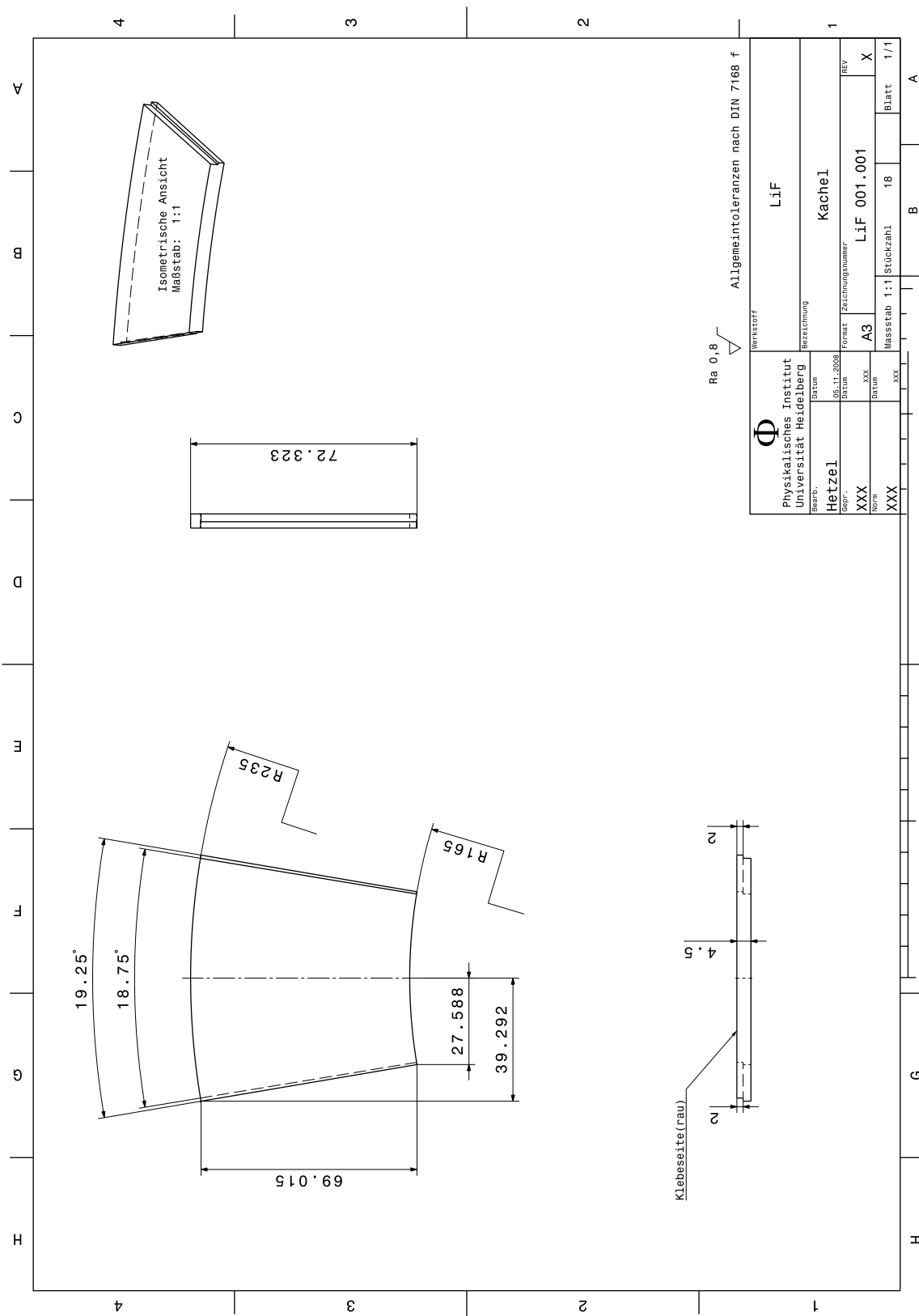
The frequency regulation consists of a microcontroller based on a ATmega128 CPU with several I/O pins and a USB connector, which makes it easy to communicate with. The software is a PI-regulator with additional features like a maximum power cutoff to not overload the motor, security shut down when the rotary frequency can't be measured reliably and in-depth log output. The controller regulates the voltage output of the chopper's power supply via a 16bit DAC and measures the frequency of the chopper disc using a photoelectric relay with 60 pulses per turn.

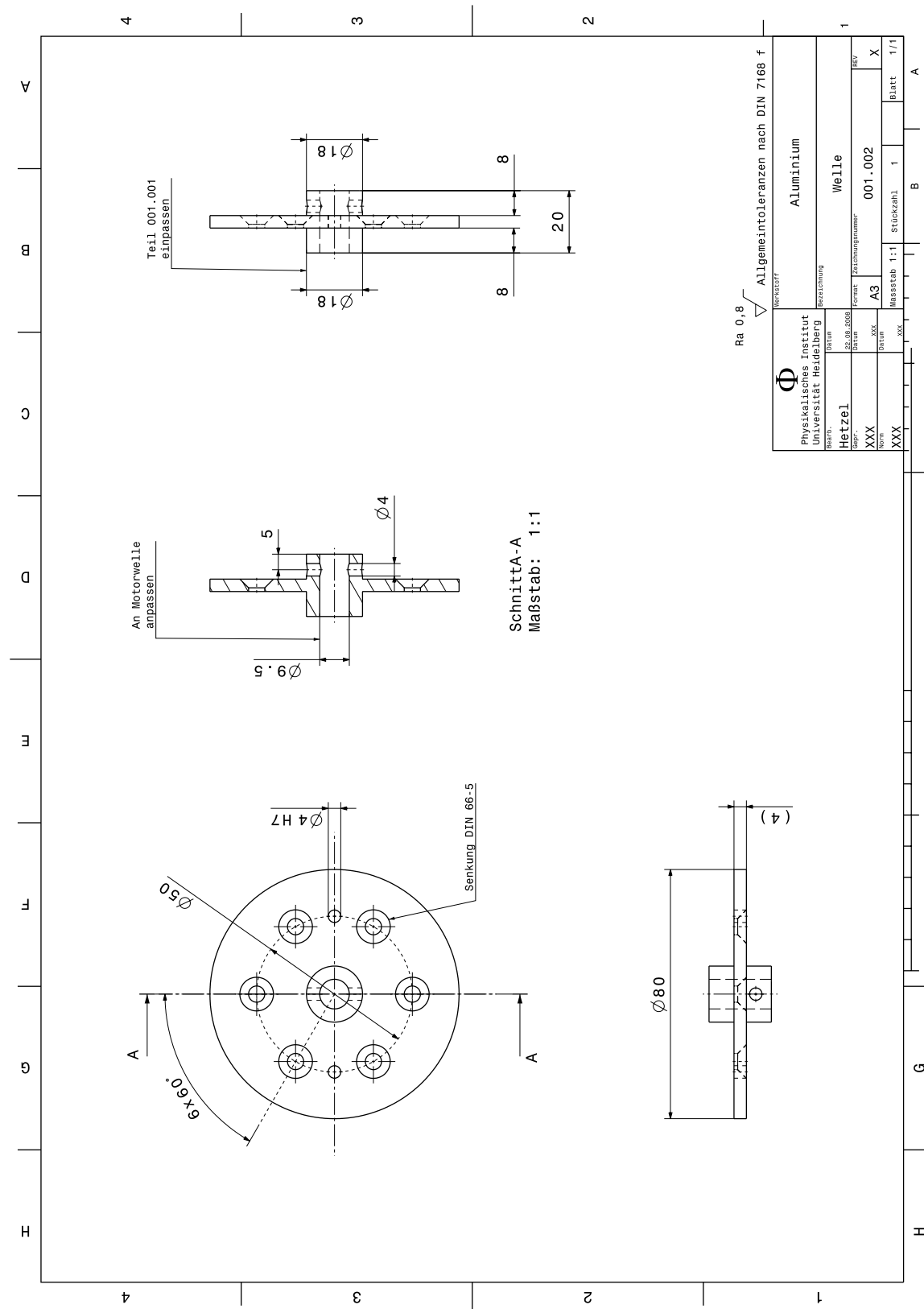
The theoretically achievable precision for the frequency measurement is limited by the count statistics we can get during one measurement. The duration of one measurement is 3s. At  $f = 80$  Hz and 60 pulses per turn the relative error amounts to

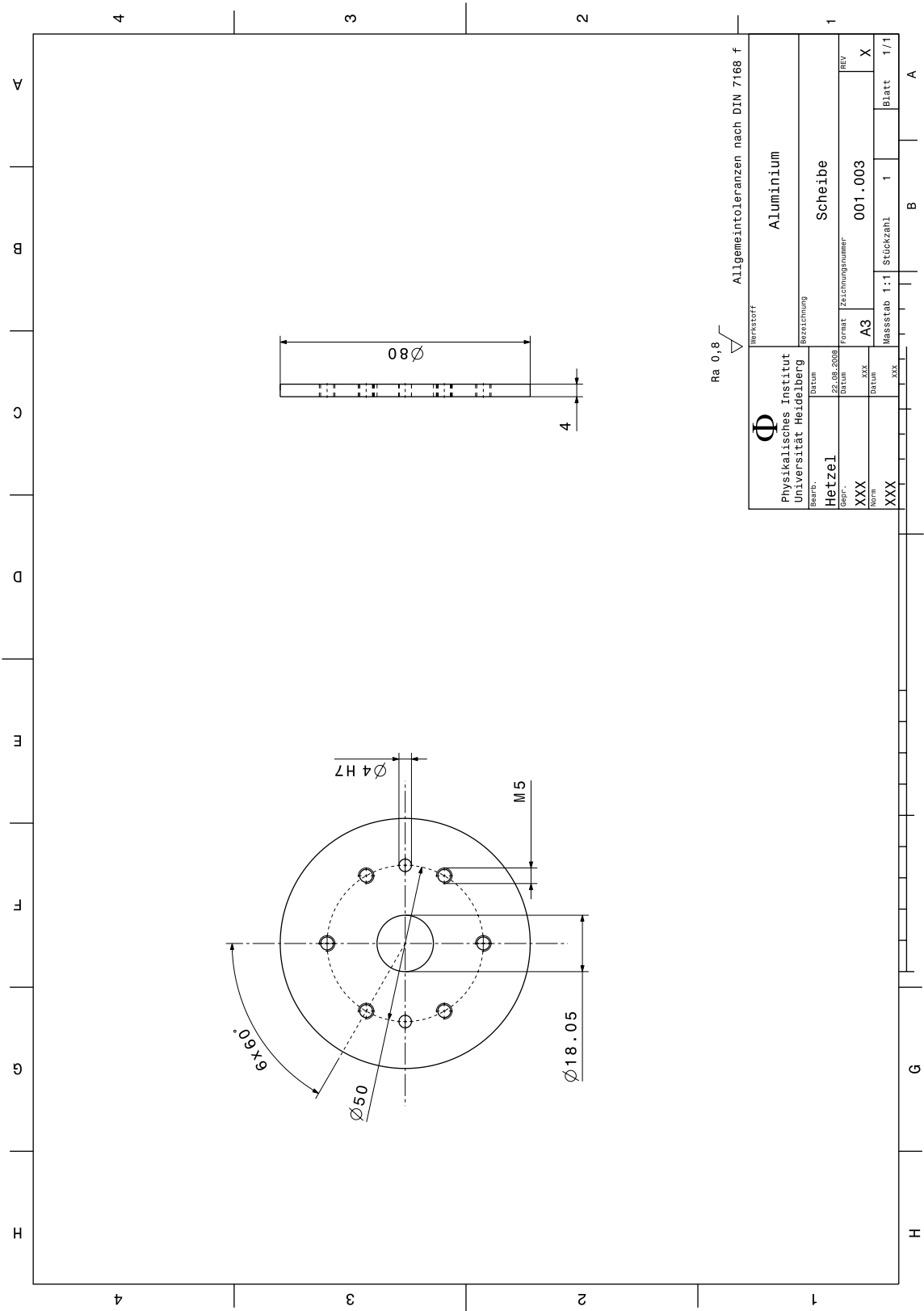
$$\frac{\Delta f}{f} = \frac{1}{3 \cdot 60 \cdot f} = 6.9 \cdot 10^{-5} \quad (\text{A.1})$$

which is well suited for the planned chopper precision. During operation, we achieve a relative FWHM of  $2.1 \cdot 10^{-4}$ . Full technical documentation is available in the source code repository of the Perkeo group.









Ra 0,8  $\sqrt{\text{A}}$  Allgemeineintoleranzen nach DIN 7168 f

Physikalisches Institut Universität Heidelberg		Werkstoff	Aluminium
Bezeichnung	Scheibe		
Seitb.	Datum	Format	Zuschlagsnummer
Hetzl	22.08.2008	A3	001.003
Gepr.	XXX	REV	X
Norm	XXX	Blatt	1/1
XXX	XXX	Massstab 1:1	Stückzahl 1

## A.4 Vibration Measurement

The chopper disc was balanced to the quality factor G 6.3 (ISO 1940). We measured the vibration on the chopper case at two positions shown in figures A.2 and A.3. None of the resonances lie within the range of nominal operation, which is between 4900 and 6000 rpm.

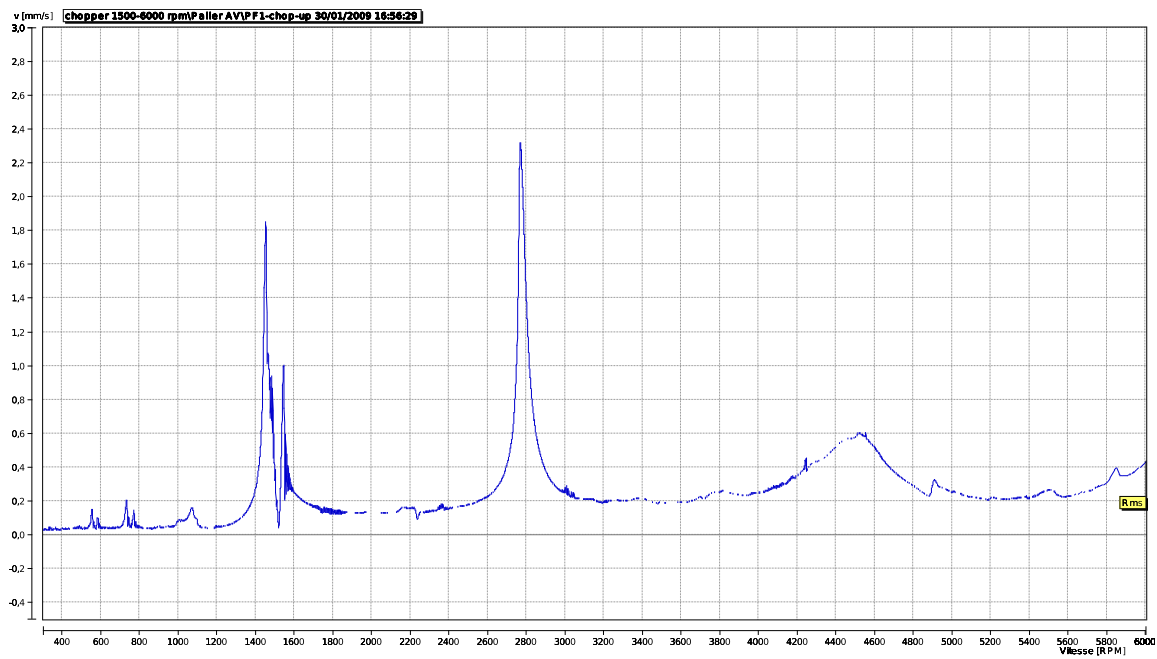


Figure A.2: Chopper resonances measured near the vacuum feed-through.

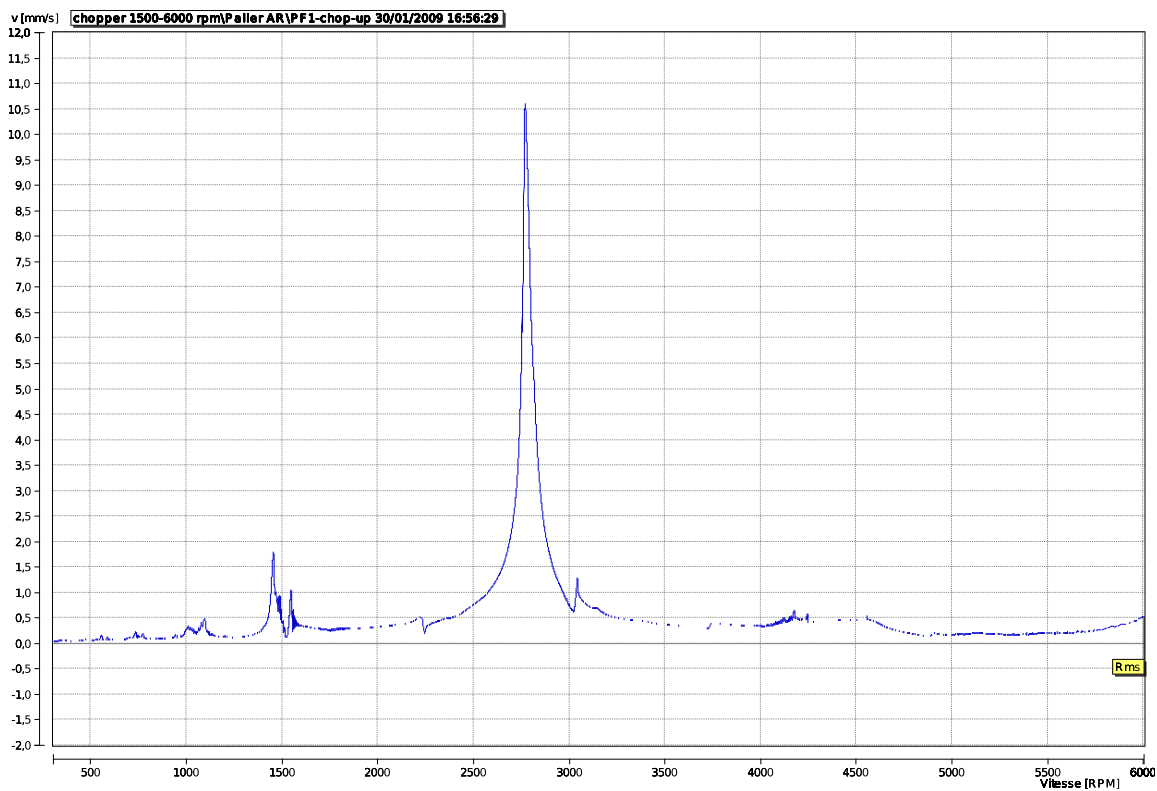


Figure A.3: Chopper resonances measured near the motor flange.

# Bibliography

- [Abe97] Hartmut Abele. *Phys. Lett. B*, 407:212, 1997.
- [Abe02] Hartmut Abele. *Phys. Rev. Lett.*, 88, 2002.
- [Abe06] Hartmut Abele. *Nucl. Instr. and Meth.*, 562:407–417, 2006.
- [Abe08] Hartmut Abele. The neutron. its properties and basic interactions. *Prog. Particle Nucl. Phys.*, 60, 2008.
- [Ams08] C Amsler. Review of particle physics. *Phys. Lett.*, B667:1, 2008.
- [Aqu91] M. Aquino. *Phys. Lett. B*, 261:280, 1991.
- [Arz00] S. Arzumanov. *Phys. Lett. B*, 483:15, 2000.
- [Bop86] P. Bopp. Beta decay asymmetry of the neutron and ga/gv. *Phys. Rev. Lett.*, 56:919, 1986.
- [Dub08] D. Dubbers. A clean, bright, and versatile source of neutron decay products. *Nucl. Instrum. Meth. A*, 596:238–247, 2008.
- [HM52] C. T. Hibdon and C. O. Muehlhause. Internal conversion of neutron capture  $\gamma$ -rays. *Phys. Rev.*, 88(4):943–944, Nov 1952.
- [HT05] J. Hardy and J.S. Towner. *Phys. Rev. C*, 71, 2005.
- [ILL03] ILL. Neutron Data Booklet, Juli 2003.
- [JT57] J. D. Jackson and S. B. Treiman. *Phys. Rev.*, 106:517–521, 1957.
- [Kno79] G. F. Knoll. *Radiation Detection and Measurement*. John Wiley and Sons, 1979.
- [Lia97] P. Liaud. *Nucl. Phys. A*, 612:53, 1997.
- [Lon80] M. A. Lone. MeV Neutron production from thermal neutron capture in Li and B compounds. *Nuclear Instruments and Methods*, 1980.
- [Mam89] W. Mampe. *Phys. Rev. Lett.*, 63:593, 1989.
- [MP75] R. N. Mohapatra and J. C. Pati. *Phys. Rev. D*, 11:566, 1975.
- [Mun06] Daniela Mund. PhD thesis, University of Heidelberg, 2006.

- 
- [Mä] Bastian Märkisch. Private communication.
- [Mä06] Bastian Märkisch. *Das Spektrometer Perkeo III und der Zerfall des freien Neutrons*. PhD thesis, University of Heidelberg, 2006.
- [Pic00] A. Pichlmaier. *Nucl. Instrum. Methods Phys. Res., Sec. A*, 440:517, 2000.
- [Rav95] Carsten Raven. Diploma thesis, 1995.
- [Rei99] Jürgen Reich. *Winkelkorrelationen im Zerfall polarisierter Neutronen*. PhD thesis, University of Heidelberg, 1999.
- [RGF67] H. Rauch, F. Grass, and B. Feigl. Ein neuartiger Detektor für langsame Neutronen. *Nuclear instruments and methods*, 74:153–156, 1967.
- [RMS06] M. J. Ramsey-Musolf and S. Su. Low energy precision test of supersymmetry, 2006.
- [Ros04] L. Rosta. *Physica B*, 350:711–716, 2004.
- [SBNC06] N. Severijns, M. Beck, and O. Naviliat-Cuncic. Tests of the standard electroweak model in beta decay, 2006.
- [Ser05] A. Serebrov. Measurement of the neutron lifetime using a gravitational trap and a low-temperature fomblin coating. *Phys. Lett. B*, 605:72, 2005.
- [Wan] Wang Xiangzun. Private communication.
- [Wil82] D. H. Wilkinson. *Nucl. Phys. A*, page 474, 1982.
- [Yer97] B. G. Yerozolimsky. *Phys. Lett. B*, 412:240, 1997.

# Acknowledgements

Many people supported me during this thesis. In this non-exhaustive list, I'd like to thank:

**Professor Hartmut Abele**

for the opportunity to work on this project.

**Professor Dirk Dubbers**

for his advice and discussions.

**Dr. Bastian Märkisch**

for the mentoring during my thesis.

**Wang Xiangzun and Holger Mest**

for fruitful discussions, advice and support.

**Dr. Torsten Soldner**

for support and sharing of his knowledge.

**Dr. Ulli Köster**

for advice and many interesting facts about the ILL and the reactor.

**Günther Stahl, Jessica Riedinger and Stefan Hetzel**

for technical support regarding chopper disc, LiF tiles and CAD.

**Didier Berruyer and Pascal Lachaume**

for their technical support.

**Dr. Ulrich Schmidt**

for advice regarding Mathematica.



# Erklärung

Ich versichere, daß ich diese Arbeit selbstständig verfasst habe und keine anderen als die angegebenen Quellen und Hilfsmittel benutzt habe.

Heidelberg, den 4. August 2009